Acta Materialia 288 (2025) 120852

Contents lists available at ScienceDirect

Acta Materialia

journal homepage: www.elsevier.com/locate/actamat

Hydrogen accommodation and its role in lattice symmetry in a TiNbZr medium-entropy alloy

Chengguang Wu [a], Yilun Gong [a,b,*], Chang Liu [c], Xuehan Li [c], Gökhan Gizer [d], Claudio Pistidda [d], Fritz Körmann [a,e,f], Yan Ma [a,g,*], Jörg Neugebauer [a], Dierk Raabe [a]

[a] Max Planck Institute for Sustainable Materials, Max-Planck-Straße 1, 40237, Düsseldorf, Germany
[b] Department of Materials, University of Oxford, Parks Road, Oxford OX1 3PH, UK
[c] Center for Alloy Innovation and Design (CAID), State Key Laboratory for Mechanical Behavior of Materials, Xi'an Jiaotong University, 710049, Xi'an, China
[d] Helmholtz-Zentrum Hereon, Max-Planck-Straße 1, 21502 Geesthacht, Germany
[e] Interdisciplinary Centre for Advanced Materials Simulation (ICAMS), Ruhr-Universität Bochum, 44801, Germany
[f] Institute for Materials Science, University of Stuttgart, Pfaffenwaldring 55, 7056, Germany
[g] Department of Materials Science and Engineering, Delft University of Technology, Mekelweg 2, 2628 CD Delft, the Netherlands

ARTICLE INFO

Keywords:
Medium-entropy alloys
Microstructural evolution
Tetragonality
Hydrogen accommodation
Ordering effect

ABSTRACT

Refractory medium/high-entropy alloys (M/HEAs) are emerging as promising alternative materials for hydrogen storage and hydrogen combustion engines due to their favorable thermodynamic and kinetic conditions for hydrogen accommodation (for the former) and promising high-temperature mechanical properties (for the latter). A better understanding of hydrogen-metal interactions is necessary to advance the development of this material class, thus helping leverage hydrogen-based applications. Here we reveal the microstructural evolution of a TiNbZr MEA by *in-situ* synchrotron high-energy X-ray diffraction (HEXRD) during hydrogenation in pure H_2 gas at atmospheric pressure. At 500 °C, dissolved hydrogen atoms gradually expand the crystal lattice isotropically, and the body-centered cubic crystal remains stable up to a hydrogen concentration of ~46.4 at.%. The thermodynamics of hydrogen accommodation associated with experimental observations in the crystal lattice is elucidated using density functional theory (DFT). The calculations suggest that tetrahedral interstitial sites are the thermodynamically favorable positions for hydrogen accommodation in both cases (i) for a single hydrogen in the special quasirandom structure supercell and (ii) at a high hydrogen concentration (~45.4 at.%). In the latter case, hydrogen interstitials are randomly distributed on the tetrahedral sites. Upon cooling, it is observed that the body-centered cubic lattice transforms to a body-centered tetragonal structure. The DFT calculations show that this change is related to the ordering distribution of hydrogen interstitials within the TiNbZr lattice. By combining *in-situ* HEXRD experiments and DFT calculations, the study provides fundamental insights into hydrogen accommodation in the interstitial positions and its impact on the lattice symmetry in TiNbZr MEA.

1. Introduction

The hydrogen economy can provide sustainable solutions to reducing the use of fossil fuels, thus mitigating CO_2 emissions and combating global warming [1–3]. Such a paradigm shift necessitates the rapid development of advanced metallic alloys, particularly for hydrogen storage and transportation as well as for applications in which safety-critical components where hydrogen is used as an energy carrier (for example, in hydrogen combustion engines or electrochemical energy-related devices) are exposed to hydrogen-rich reactive atmospheres [2,4,5]. Body-centered cubic (BCC) refractory medium/high-entropy alloys (M/HEAs), as an emerging alloy class, have been considered to be potential candidates for hydrogen storage and high-temperature applications [6–12]. The compositional complexity of M/HEAs systems provides a broad spectrum of mechanical and functional properties for various applications [7,13]. For example, Ti-based refractory M/HEAs stand out, exhibiting decent room-temperature tensile ductility [10]. Moreover, a carefully adjusted composition of Ti-based refractory M/HEAs shows promising performance for hydrogen storage, with a hydrogen-to-metal ratio of ~2.5 and favorable thermodynamics and kinetics required for rapid and low-barrier hydrogen absorption and desorption [5,14,15]. Both

* Corresponding authors.
E-mail addresses: y.gong@mpie.de, yilun.gong@materials.ox.ac.uk (Y. Gong), y.ma@mpie.de, y.m.ma@tudelft.nl (Y. Ma).

https://doi.org/10.1016/j.actamat.2025.120852
Received 3 September 2024; Received in revised form 16 January 2025; Accepted 19 February 2025
Available online 20 February 2025

thermodynamic and kinetic aspects are fundamental in the field of hydrogen storage. Increasing the concentrations of trapping sites and stored hydrogen atoms is an essential thermodynamic requirement, yet they are insufficient as standalone design targets for hydrogen storage. Additionally, applications require adequately tailored reaction and diffusion kinetics enabling tunable hydrogen absorption and release, pertaining to the targeted application scenarios.

The interactions between hydrogen and the host alloying atoms that constitute refractory M/HEAs play a salient role in that respect [14,16,17]. Hydrogen was reported to accommodate to the tetrahedral sites of the face-centered cubic (FCC) hydride phase during hydrogenation [5,17]. In contrast to such hydrogen storage considerations (where both hydrogen storage capacity and remobilization upon dehydrogenation are essential criteria), it is also well known that hydrogen-induced embrittlement can drastically and abruptly reduce the lifespan of metallic components under mixed mechanical, thermal and chemical boundary conditions, already with as little as a few wppm diffusible hydrogen present [18–22]. Hydrogen has a high tendency to segregate to grain boundaries driven by the reduction of the free energy of the system, thereby reducing the cohesion between grains and leading to crack formation and propagation along grain boundaries and catastrophic failure of metallic structures [23,24]. Hence, an in-depth understanding of the hydrogen-metal interaction associated with hydrogen ingression becomes critical to the design of novel metallic alloys that might be potentially applicable to the hydrogen economy [25–28,98]. However, one major problem to making profound progress in this field lies in directly observing the dynamic interaction of hydrogen atoms with metals, due to the challenging intrinsic features of hydrogen, *e.g.* it is the lightest element (1.008 u), has the smallest atomic radius (53 pm), and highest diffusion coefficient in metals ($\sim 10^{-10}$ m^2/s at ~500 °C) [29,30].

In this study, the time-resolved microstructural transitions and associated hydrogen accommodation in an equiatomic TiNbZr alloy were quantitatively probed using *in-situ* synchrotron high-energy X-ray diffraction (HEXRD) during heat treatments in H_2 and Ar atmosphere at 500 °C under atmospheric pressure. The reasons for selecting the equiatomic TiNbZr alloy as a model material for this study are as follows: (1) Most of the alloys that have been considered so far for hydrogen-related applications belong to the TiNbZr alloy family and variants of it, *e.g.*, TiNbZr-Ta, TiNbZr-V, and TiNbZr-HfTa (see supplementary materials **Table S1**) [6,7,10,31–33]. (2) Ti, Zr, and Nb are the three most critical elements in this M/HEA class, where Ti and Zr are the major elements in more than 80 % of the reported M/HEAs systems for hydrogen storage due to their high affinities to hydrogen, and Nb is the main element to stabilize a BCC crystal structure (a low packing density of 68 %, facilitating hydrogen diffusion). (3) Compared with the quaternary and quinary alloys mentioned above, the TiNbZr alloy is a system that is on the one hand common to most of these more complex alloys. On the other hand, it is thermodynamically their simplest possible phenotype. Both features qualify this ternary system as a core alloy for studying hydrogen effects on the microstructural transition using both experiments and simulations, to provide an in-depth understanding of the underlying mechanisms along the spirit 'as simple as possible but not simpler'. (4) This alloy reveals a hydrogen-to-metal ratio of up to ~1.9, which is attractive for hydrogen storage. The advantage of the HEXRD method lies in the capability of providing the real-time evolution of lattice structures in a statistically representative volume with an excellent time resolution (down to the sub-second regime) [34,35]. Additionally, density functional theory (DFT) calculations were employed to reveal the thermodynamically favorable sites for hydrogen in the crystal lattice. For a fundamental understanding of various properties of metal-hydrogen systems, such as phase stability, fracture toughness, and hence structural integrity, it is essential to know the relationship between hydrogen concentration and site occupancy. Such a combination of experimental and computational results offers new insights into the hydrogen-metal interactions in refractory MEAs and their corresponding impacts on the lattice structure.

2. Materials and methods

2.1. Materials

The equiatomic TiNbZr alloy was prepared using high-purity elements (99.9 %) in an arc-melting furnace with a water-cooled copper crucible. To prevent the alloy from oxidation during melting, the furnace was filled with high-purity Ar (99.999 %), and an oxygen-getter material (*i.e.*, a piece of pure Ti) was placed in the furnace. Fine TiNbZr powders (dendrite microstructure) with a median particle size of 30 μm were prepared from the ingot by gas atomization (Angstrom Sciences, Germany). The oxygen content of the pristine TiNbZr powder is 0.81 at.% as determined by thermal desorption spectroscopy (TDS). The potential influence of oxygen contamination on hydrogen storage and release kinetics might consist of several aspects: (1) A reduction in hydrogen storage capacity because oxygen occupies the same sites in the host crystal otherwise used by hydrogen; (2) The surface oxidation with a dense structure might act as an additional entry and release barrier for hydrogen [36–38]. However, the latter point is of moderate concern as the high solubility of oxygen in this alloy (*i.e.*, ~8 at.% oxygen for β-Ti) implies that oxide formation is unlikely in the present alloy [39].

2.2. Microstructure characterization

The microstructure of the pristine and hydrogen-charged powders was characterized by a combination of backscattered electron (BSE) imaging and electron backscatter diffraction (EBSD) techniques in a Zeiss Sigma 500 scanning electron microscope (SEM). To observe the cross-sectional area of the TiNbZr powders, they were embedded in a conductive phenolic resin contacting carbon fillers (Polyfast Struers) and then ground with sandpapers with grit sizes ranging from 400 to 4000. Subsequently, the samples were polished with 50 nm colloidal silica (OPS) suspension mixed with hydrogen peroxide (H_2O_2, 30 vol.%). The EBSD measurements were performed with a step size of 50 nm under an accelerating voltage and probe current of 15 kV and 7 nA and the collected data were analyzed using the software OIM Analysis™ V8.0. In addition, the local chemistry of powders was probed by electron dispersive spectroscopy (EDS) in the SEM. Moreover, the surface morphology of the TiNbZr powders was characterized by secondary electron (SE) imaging. In this case, the TiNbZr powders were directly dispersed on a copper tape holder and coated with 4-nm thick carbon. To analyze the local crystallographic information of the hydrogen-charged specimen, the selected area electron diffraction (SAED) pattern was collected using transmission electron microscopy (TEM). The TEM lamella was prepared using focused ion beam (FIB, FEI Helios NanoLab 600i dual-beam FIB/SEM instrument). The TEM analysis was conducted using a Titan Themis instrument G2 300 operated at 300 kV.

2.3. In-situ synchrotron high-energy X-ray diffraction

In-situ synchrotron high-energy X-ray diffraction (HEXRD) was employed to study the hydrogenation behavior of the TiNbZr alloy. The HEXRD experiments were conducted at the Powder Diffraction and Total Scattering Beamline P02.1 of PETRA III at Deutsches Elektronen-Synchrotron (DESY) in Hamburg, Germany [40]. Fig. 1 schematically shows the HEXRD experimental setup. A chemical reaction cell for gaseous charging was placed between the incident X-ray beam and a two-dimensional detector. TiNbZr powders (3–5 mg) were loaded into a single-crystal sapphire capillary with an inner diameter of 0.6 mm, which was assembled in the reaction cell [41,42]. A hot air blower (Oxford Instrument) was employed to heat the sample. The temperature of the sample was measured using a type K thermocouple. Both pure H_2 (for hydrogenation) and Ar (as reference) gases with a purity of 99.999 % were used in the experiments at a pressure of 1 bar. The flow rate was

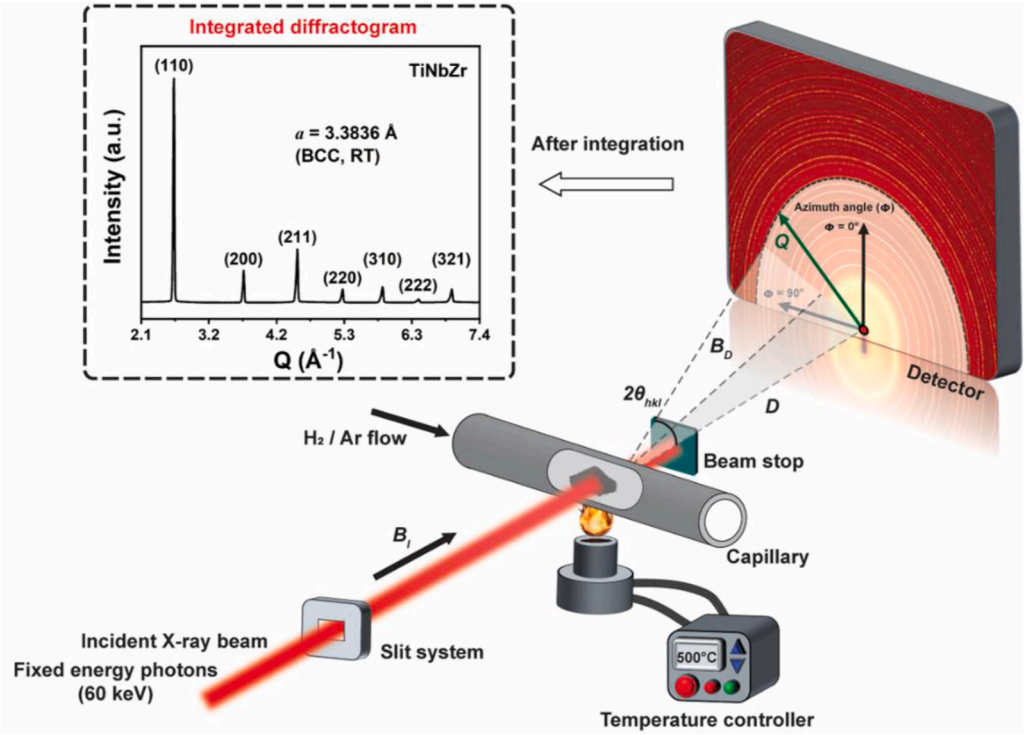

Fig. 1. Schematic illustration of the experimental setup of the *in-situ* synchrotron high-energy X-ray diffraction (B_I and B_D indicate the vectors of the incident and diffracted beams, respectively; D is the distance between the sample and the two-dimensional detector; $2\theta_{hkl}$ indicates scattering angle; Q stands for the scattering vector). Insert figure (marked by the black dash box) shows the integrated diffractogram of pristine TiNbZr powders at 30 °C, demonstrating a single body-centered cubic (BCC) structure with a lattice parameter of 3.3836 Å.

kept at 50 mL/min, which was controlled by a mass flow controller. Prior to heating, the capillary was purged with the H_2 or Ar gas for 30 mins to remove residual air in the cell for the hydrogenation or reference experiments, respectively. Then, the sample was heated to 500 °C with a heating rate of 0.3 °C/s and subsequently held at 500 °C for ~1800 s, followed by cooling the cell in air. During the heat treatment, the HEXRD patterns were recorded to investigate the real-time microstructure evolution. The beam energy of the X-ray was fixed at 60 keV to obtain a monochromatic X-ray with a wavelength of ~0.207 Å. The beam size of the incident beam was 1 mm × 1 mm. The Debby-Scherrer patterns were recorded every second by the fast area detector Varex XRpad 4343CT (2880 pixels × 2880 pixels, with a pixel size of 150 μm × 150 μm). Thanks to the 'powder' feature of the sample, the pattern revealed isotropic scattering behavior along the azimuth angle. Thus, half-ring configuration was employed, *i.e.*, half of the Debby-Scherrer rings were captured. In this case, the crystal information at a high scattering vector (with a Q_{max} up to ~15 $Å^{-1}$) could be accessed simultaneously.

The HEXRD patterns were integrated over an azimuth angle of 180° into intensity-scattering vector Q plots using the GSAS-II software [43]. The sequential Rietveld refinement was conducted for selected data points to deconvolute the HEXRD patterns and quantitatively analyze the fraction of individual phases as well as their corresponding lattice parameters. The values of the weighted profile R-factor (R_{wp}) for all the refinements were below 8.0 %, demonstrating the high reliability of the results obtained. Furthermore, the pair distribution function (PDF) profiles ($G(r)$) were obtained from the total scattering data with a Q_{max} of around 15 $Å^{-1}$ via the Fourier transform of the structural function ($S(Q)$). The peak widths (σ) and interatomic distances of the first three coordination shells were also determined from the PDF analysis.

2.4. Density functional theory (DFT) calculations

DFT calculations were performed to identify and verify the experimentally observed lattice structures of the TiNbZr alloy charged with hydrogen. The DFT calculations used the projector augmented wave (PAW) method [44] as implemented in the Vienna *Ab-initio* Simulation Package (VASP) [45,46]. The provided PAW potentials [47] were employed, treating the $4p^6 4d^4 5s^1$, $3p^6 3d^3 4s^1$, $4s^2 5s^1 4d^6 4p^3$, and $1s^1$ orbitals as valence electrons for Nb, Ti, Zr, and H, respectively. The generalized gradient approximation (GGA) with Perdew-Burke-Ernzerhof (PBE) [48] parameterization was used for the exchange-correlation function. All calculations were performed using a 500 eV kinetic-energy cutoff and a 6 × 6 × 6 k-point mesh according to the Monkhorst-Pack scheme [49,50]. Fermi-Dirac smearing with an electronic temperature of 0.07 eV (corresponding to about 800 K) was used. Electronic minimization and stress relaxation with total energy convergence parameters of 2×10^{-4} meV/atom and 2×10^{-3} meV/atom were employed respectively. A 3 × 3 × 3 MEA BCC conventional supercell with 54 metallic atoms was used in the simulation, which allows to conduct calculations for an equiatomic composition. The supercell was constructed using the special quasirandom structure (SQS) method [51]. An averaged, effective solution enthalpy, ΔH_{sol} (per hydrogen atom) was calculated by,

$$\Delta H_{sol} = \frac{E_{M+nH} - E_M}{n} - \mu_H \quad (1)$$

where n indicates the number of hydrogen atoms in the supercell. The total energy E for each supercell was calculated allowing for stress relaxation (*i.e.*, supercell volume/shape and atomic positions). The chemical potential of hydrogen, μ_H, was calculated as half of the total energy of the H_2 molecule.

3. Results

3.1. Microstructure of the pristine TiNbZr sample

The pristine TiNbZr sample exhibits a spherical morphology (Figs. 2a-b) and the average diameter of the particles is 23.56±0.82 μm, as quantified by analyzing more than 200 particles (Fig. 2c). As shown in the cross-sectional SEM image (Fig. 2d), the pristine powders reveal a typical dendritic microstructure formed during solidification after the atomization process. Nb accumulates in the dendritic regions (with an area fraction of 52 %) while the interdendritic regions (with an area fraction of 48 %) are enriched in Ti and Zr (Figs. 2d-e). Such a dendritic microstructure was also observed in as-cast refractory M/HEAs [32,52,53]. The segregation behavior is attributed to the large solidification temperature region (~300 °C) among these elements [54,55]. The tendency of Ti and Zr to undergo co-segregation is mainly due to the lower mixing enthalpy between these two elements (0 kJ/mol as compared to 2 kJ/mol for Ti-Nb and 4 kJ/mol for Zr-Nb) [53,56]. The composition of the dendritic region was quantified by EDX as $Ti_{33.38}Nb_{31.70}Zr_{34.92}$ (in at.%), while the composition of the interdendritic region was determined to be $Ti_{31.29}Nb_{37.46}Zr_{31.25}$ (in at.%, **Table S2**). Such a small chemical fluctuation has negligible effects on phase stability, as confirmed by HEXED measurements (in Section 3.2). Despite the local chemical fluctuation, the average concentration is consistent with the nominal composition (**Table S2**). The sample possesses randomly oriented grains with an average grain size of 8.83±2.74 μm (Fig. 2f). Additionally, the high-angle grain boundaries constitute a major part of the grain boundaries, accounting for 83.8 %, while low-angle grain boundaries occupy 16.2 %.

3.2. Hydrogen solution in the TiNbZr alloy

The hydrogenation behavior of the TiNbZr powder was investigated by employing *in-situ* HEXRD during hydrogen charging. Figs. 3a and c show the overall evolution of the integrated HEXRD peaks of TiNbZr samples upon heat treatment in pure H_2 (Fig. 3b) and Ar (as a reference, Fig. 3d). The HEXRD confirms that the pristine sample possesses a single body-centered cubic (BCC, $Im\bar{3}m$ space group) crystal structure. In both cases, an evident peak shift to a lower scattering vector (Q) is observed during heating from room temperature to 500 °C, suggesting an increase in interplanar spacing of the crystal lattice. During the isothermal treatment at 500 °C, a further systemic peak shift to a lower Q and peak broadening are observed for the sample treated in pure H_2 (Fig. 3a). In comparison, no change in the diffraction peaks is found in the reference sample that treated in Ar under the same heat treatment (Fig. 3c). This fact confirms that the peak shift and broadening in the sample treated in H_2 is related to hydrogen ingression in the crystal lattice, resulting in lattice expansion. Upon cooling, the sample treated in H_2 reveals further peak broadening with gradual loss of the symmetry of diffraction peaks

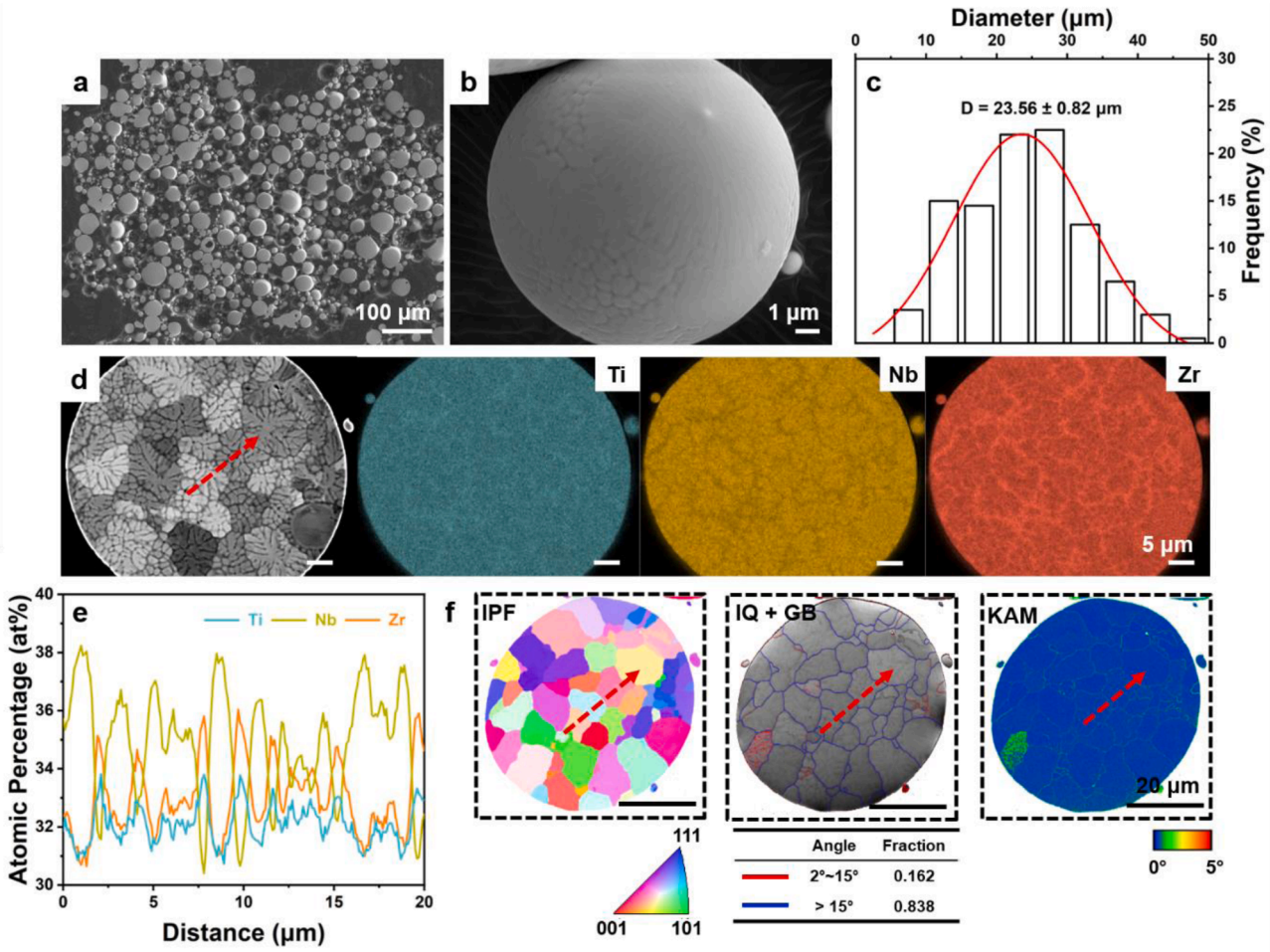

Fig. 2. Secondary electron images of (a) TiNbZr powder and (b) a particle at high magnification in the pristine state. (c) The corresponding size distribution measured from (a) using the software ImageJ over 200 particles. (d) Backscattered electron imaging of a particle and the corresponding individual elemental maps of Ti, Nb, and Zr probed by electron dispersive spectroscopy. (e) Elemental distribution across dendrites along the red arrow in (d). (f) Inverse pole figure (IPF), image quality overlaid with grain boundaries (IQ + GB), and kernel average misorientation (KAM) maps of the particle probed by the electron backscatter diffraction. The red arrow in (f) represents the same line scan in (d).

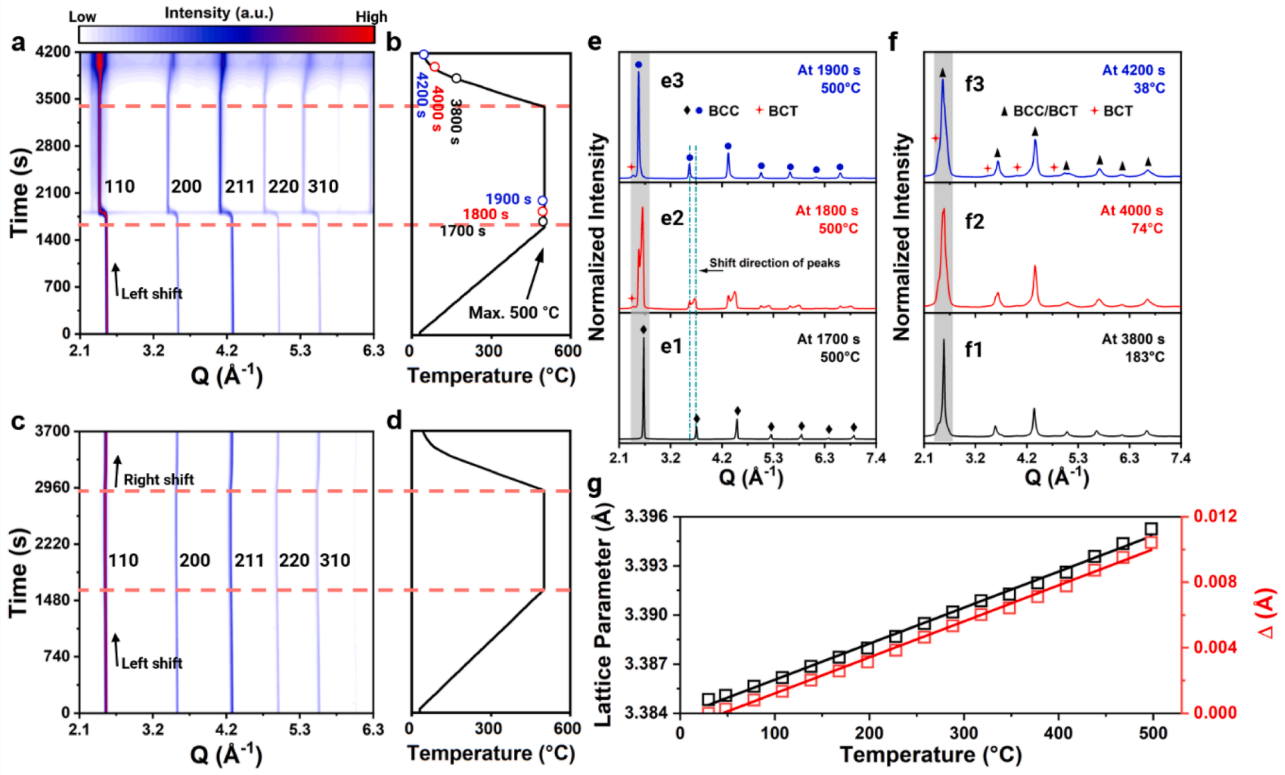

Fig. 3. Contour maps of the diffraction intensity integrated over the azimuth angle of 180° probed by *in-situ* high-energy X-ray diffraction (HEXRD) during heat treatments of the TiNbZr alloy in (a) H_2 and (c) Ar, (b) and (d) the corresponding temperature profiles. HEXRD profiles of the sample treated in H_2 for (e1) 1700 s, (e2) 1800 s, (e3) 1900 s (at the beginning of the isothermal process at 500 °C), (f1) 3800 s, (f2) 4000 s, and (f3) 4200 s (upon cooling). (g) Lattice parameter and the relative change (Δ) in the lattice parameter of the sample during heating from room temperature to 500 °C in H_2.

(Fig. 3f), suggesting the formation of a crystal structure with low symmetry. In contrast, the reference sample treated in Ar reveals only thermal contraction [57,58], implying that the TiNbZr alloy remains a BCC structure in Ar.

The response of crystal structures to heat treatment in these two samples was further studied by analyzing the pair distribution function (PDF) profiles (**Figs. S3** and **S4**). This method reveals the probability of finding two atoms within the alloy by a distance *r*, based on the Fourier transformed from the reciprocal space to the real space [59]. For the reference sample, no obvious change is detected in the PDF profiles along the whole heat treatment. In contrast, the loss of long-range correlations is observed in the sample treated in H_2, particularly during the onset of isothermal treatment and subsequent cooling processes, indicating the disordering of the metal matrix [59]. Such disorder implies possible transitions of the crystal structure, which will be analyzed in detail in the following sub-chapters.

3.2.1. *Evolution of lattice structure upon heating*

During heating the sample in H_2 up to 500 °C, the lattice parameter increases linearly as a function of temperature (Fig. 3g). Such linear behavior is mainly due to an increase in lattice vibration stimulated by increasing temperature [57,58]. The linear thermal expansion of the TiNbZr alloy is subtle (Δ = 0.010 Å) with a thermal expansion coefficient α of 6.578×10^{-6}/K in the temperature range from 30 °C to 500 °C. These results are consistent with those for the sample treated in Ar (Δ = 0.012 Å, $\alpha = 6.578 \times 10^{-6}$ K^{-1}, **Fig. S6**a). This comparison suggests that no significant H_2 uptake in the sample heated in H_2 to 500 °C, which otherwise is supposed to result in an additional change in the lattice parameter.

3.2.2. *Hydrogen uptake during isothermal treatment at 500 °C*

The temperature of 500 °C has been selected for the isothermal treatment as it falls within the temperature range (300–600 °C) typical for studying phase transformations during hydrogenation (**Table S3**). It is worth noting that temperatures can impact phase stability via the change in free energy (*i.e.*, hydrogen solubility), and can also influence the kinetics of structural transitions (*i.e.*, hydrogen absorption rate) by affecting vacancy concentration and atomic diffusion [30,60,61]. During the isothermal treatment in H_2 at 500 °C, the diffraction peaks shift significantly to a lower *Q*-vector (Fig. 3a) within the initial 200 s (the elapsed time from 1700 s to 1900 s), suggesting a rapid increase in the lattice parameter. Such lattice expansion is attributed to the fast hydrogen uptake in the TiNbZr powder. There is no further shift of the diffraction peaks after the elapsed time of 2000 s (**Fig. S7**). Such stagnation indicates the saturation of the TiNbZr lattice with hydrogen atoms. To better understand the hydrogen absorption process, we next focus on the microstructure evolution within the first 200 s of the isothermal treatment. The integrated HEXRD profiles, as shown in Fig. 3e, reveal that the original BCC peaks (a = 3.391 Å at 500 °C, 1700 s) split into multiple sets of BCC peaks, and then transit back to one set of BCC peaks, yet, with a larger lattice parameter (a = 3.540 Å at 500 °C, 1900 s). A small peak at the left shoulder of the {110} reflection of the BCC phase is observed (Fig. 3e), which is most likely a sign of the occurrence of a body-centered tetragonal (BCT, I4/mmm space group) structure. Due to its small fraction (< 5.0 wt.%), this BCT peak is not taken into consideration in the Rietveld refinements for the isothermal treatment.

As exemplarily revealed in Fig. 4a, two BCC_{110} peaks are further distinguished at slightly different *Q* values (2.600 Å^{-1} and 2.615Å^{-1}) at 1700 s, suggesting two BCC structures, namely BCC-1 (85.7 wt.%, a = 3.391 Å) and BCC-2 (14.3 wt.%, a = 3.411 Å). During isothermal treatment, three more sets of BCC peaks can be deconvoluted and noted as BCC-3, BCC-4, and BCC-5 with an increase in the lattice parameters (Fig. 4b and **Figs. S8**a-c). The fraction of initial BCC-1 peaks gradually

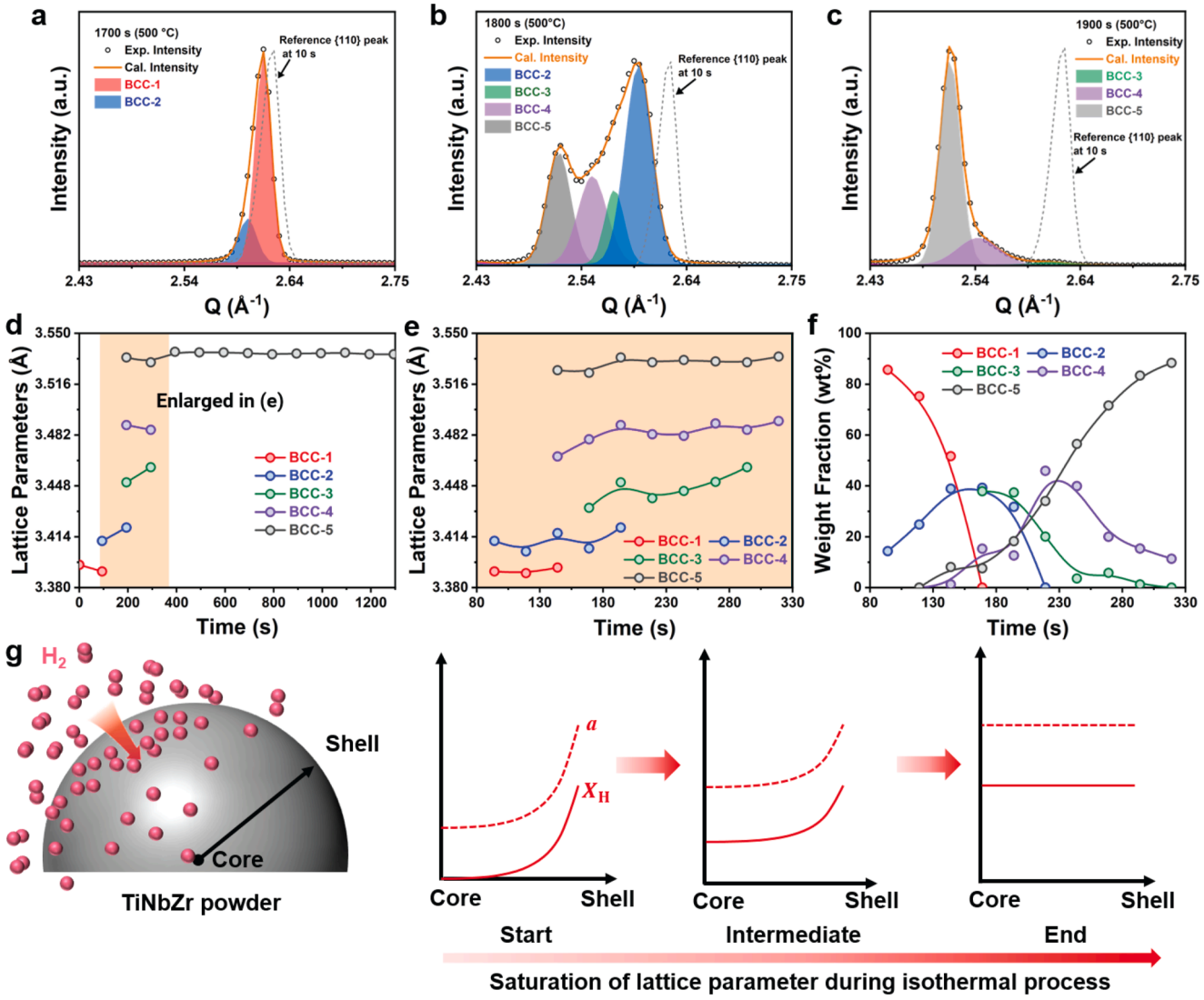

Fig. 4. Deconvoluted BCC_{110} peaks of the sample treated in H_2 at 500 °C for (a) 1700 s (starting time for the isothermal heat treatment), (b) 1800 s (isothermal holding for 100 s), and (c) 1900 s (isothermal holding for 200 s). (d) Evolution of lattice parameters (Here the initial time point (0 s) represents 1700 s during the elapsed time for the HEXRD experiment, which is the starting point for isothermal heat treatment). (e) Detailed view of lattice parameters and (f) corresponding fractions of multiple BCC structures in the early stage of the hydrogen uptake. (g) Schematic diagram showing the gradual expansion of the BCC lattices during the isothermal heat treatment process at 500 °C. a and X_H represent lattice parameter and hydrogen concentration, respectively.

decreases and disappears at 1900 s, while the fraction of BCC-2, BCC-3, and BCC-4 peaks first increases followed by a decrease (Fig. 4f), suggesting that they are the transient structures. The appearance of these transient structures with the intermediate lattice parameters is attributed to the evolution of the hydrogen concentration gradient along the radius of the particles depending on the penetration depth of hydrogen as a function of time [62,63]. As shown in Fig. 4g, when hydrogen diffuses into the particle at the beginning of the isothermal process, it generates a corresponding local gradient in the hydrogen concentration (the concentration gradually decreases from the shell to the core) [64, 65]. The solute hydrogen atoms expand the BCC lattice (below the solubility limit), resulting in an increase in its local lattice parameter, which is proportional to the hydrogen concentration and indicated by the shift of the diffraction peaks to smaller Q values in the HEXRD profiles. Due to the hydrogen concentration gradient along the diffusion path, the BCC lattice reveals a continuous variation of the lattice parameter, as shown by the asymmetric broadening of the diffraction peaks. For the sake of simplicity, in total five transition BCC structures with distinct lattice parameters were considered in the HEXRD analysis, yielding reliable Rietveld refinement results. Finally, BCC-5 becomes the predominant structure in the microstructure (88.4 wt.%, $a = 3.534$ Å, Figs. 4d and f). Additionally, only BCC-5 can be detected after 2000 s (isothermal holding for 400 s) (**Fig. S7**). This fact can be ascribed to the saturated hydrogen concentration across the whole particle. For the sample treated in Ar, the lattice parameter increases only slightly by 0.006 Å to 3.406 Å after isothermal heat treatment for about 400 s (**Fig. S6**b). Then, there is no change observed in the HEXRD profiles (**Fig. S13**).

3.2.3. *Change in lattice structure upon cooling*

Compared with the isotropic expansion of the BCC lattice during the isothermal heat treatment, the evolution of the lattice structure upon cooling back to room temperature is more complex. An asymmetric broadening of diffraction peaks is observed upon cooling, which is attributed to the presence of BCT crystal structure. The deconvoluted {110} peaks are shown in Figs. 5a-c. One BCC peak and two series of BCT peaks (BCT-1 and BCT-2) are determined upon cooling. Lattice parameters and phase fractions were extracted from the sequential Rietveld refinements (Figs. 5d-e). The fraction of the BCT-1 structure with a c/a ratio of 1.18 slowly increases to ~15.5 wt.% during the cooling process,

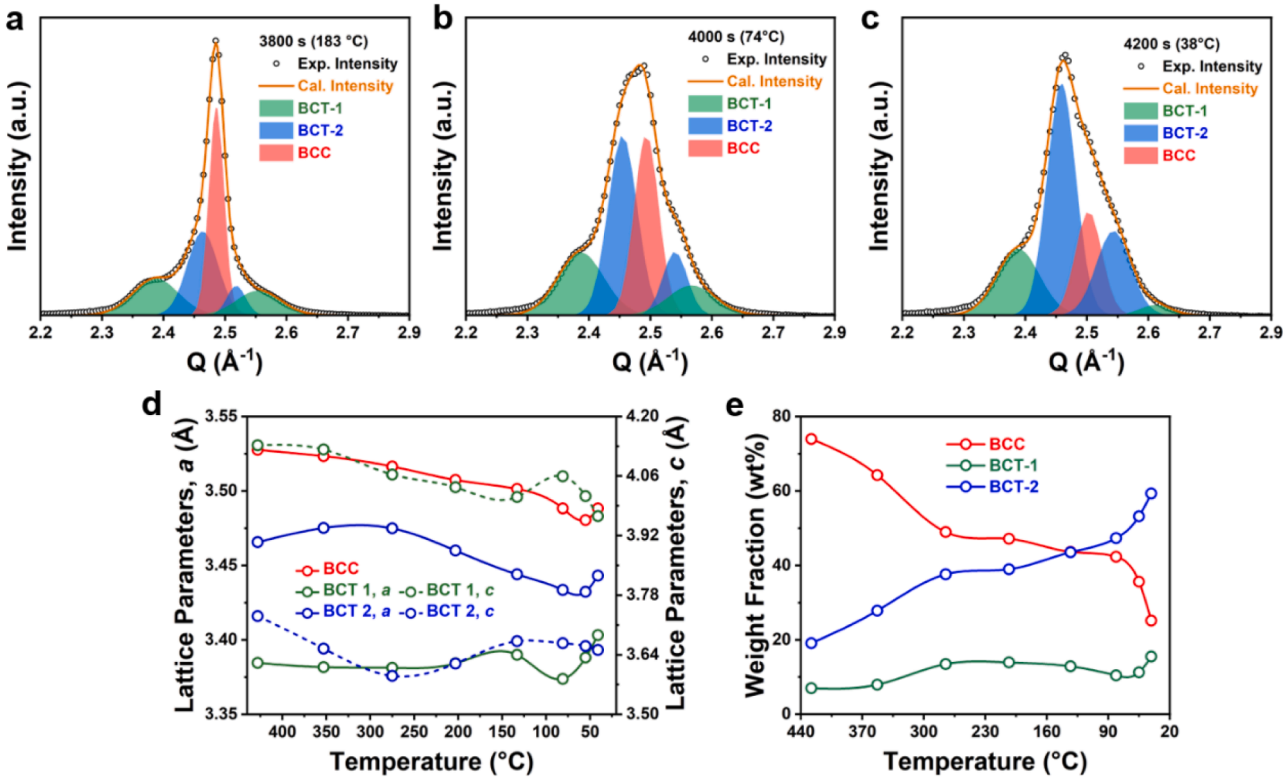

Fig. 5. Deconvoluted {110} peaks of the sample treated in H_2 during cooling at (a) 3800 s, (b) 4000 s, and (c) 4200 s (elapsed time). The evolution of (d) lattice parameters and (e) phase fractions of the deconvoluted BCC, BCT-1 and BCT-2 crystal structures.

while the fraction of the BCT-2 phase with a c/a ratio of around 1.06 reaches up to 59.3 wt.% at the final stage of cooling. In other words, in total ~80 wt.% of BCC transforms into tetragonal crystal structures upon cooling triggered by the saturated hydrogen in the BCC lattice. This transformation in crystal structure from BCC to BCT under hydrogen exposure upon cooling will be further discussed in Section 4. In the reference sample (treated with Ar), the BCC structure remains and there is no asymmetric broadening of the peaks observed (**Fig. S13**). In this case, its lattice parameter decreases linearly from 3.406 Å to 3.390 Å due to the lattice contraction induced by cooling (**Fig. S6**c). It should be noted that no FCC hydride (space group: $Fm\bar{3}m$) is found during the entire hydrogenation process under the treatment conditions in this study.

TEM was also employed to determine the tetragonality of the crystal structure after the heat treatment in H_2 (Fig. 6 and **Fig. S14**). Two overlapping diffraction patterns corresponding to the BCC and BCT crystal structures were distinguished in Fig. 6b. One set is found to stem from a BCC crystal structure with a lattice parameter of 3.395 Å, while the other indicates the occurrence of a BCT crystal structure ($a = 3.249$ Å and $c = 3.475$ Å). The corresponding BCT crystal structure is shown in the inverse fast Fourier transform (IFFT) image (Fig. 6c). The c/a ratio is approximately 1.07. Such results are consistent with the simulated patterns along the same <001> zone axis (Fig. 6d). This structural evolution from BCC to BCT results in the spontaneous symmetry breaking of the lattice structure and the discontinuous change in the lattice constant. These features meet the characteristics of a dilatation-dominated displacive phase transformation [66,67]. In this case, the ordered distribution of hydrogen interstitials, is supposed to be the main factor causing this transformation [29,68]. The above findings provide strong evidence of tetragonality within the TiNbZr matrix after the heat treatment in H_2. The underlying mechanisms for the presence of tetragonality will be discussed in the Discussion section (Section 4.2).

3.2.4. *Change in lattice volume during hydrogenation*

The relative changes in the lattice volume during the heat treatment in H_2 and Ar are shown in Fig. 7. The lattice volume is calculated with the equation, $V_t = \sum_1^n (f_i \times V_i)$, where V_t is the weighted average volume of a unit cell at time t, f_i and V_i represent the fraction and lattice volume of structure i, respectively. Here we use the change in relative volume, V_t/V_0 (V_0 is the initial lattice volume), to evaluate the evolution of the lattice volume. The lattice parameters and corresponding volumes at different time points are listed in **Table S4** and **Table S5**. The volume changes of both samples treated in H_2 and Ar are consistent during the heating to 500 °C, revealing a subtle increase by 0.627 $Å^3$, corresponding to the relative volume change of 1.010. Upon hydrogen uptake, the lattice volume is significantly increased by 4.845 $Å^3$ due to the hydrogen absorption and solution in the lattice, yielding a total relative volume change (V_t/V_0) of 1.142. This volume expansion corresponds to a hydrogen-to-metal atomic ratio of 0.865 (hydrogen concentration is determined to be 46.4 at.%), assuming that a volume expansion of 2.8 $Å^3$ is caused by introducing a single hydrogen atom in the unit cell [29,69]. Such a high hydrogen concentration is mainly attributed to the high solubility of hydrogen in group IV elements [29]. It is worth noting that a slight drop in the relative volume change happens in the sample treated in H_2 before its steep increase. This reduction in lattice volume is supposed to be due to the endothermic effect caused by hydrogen dissolution, indicating the onset of hydrogen ingress [5]. A decrease in the lattice volume is observed in both samples treated in Ar (by 0.551 $Å^3$) and H_2 (by 0.726 $Å^3$) during cooling. In the former case, the lattice volume almost recovers to its original size with a relative volume change of 1.002 in the final stage. In the latter case, such a decrease is probably due to both the thermal effect and the decrease in hydrogen solubility upon cooling.

3.3. *Microstructure after the treatment in H_2*

The microstructure of the TiNbZr sample after the treatment in H_2 is

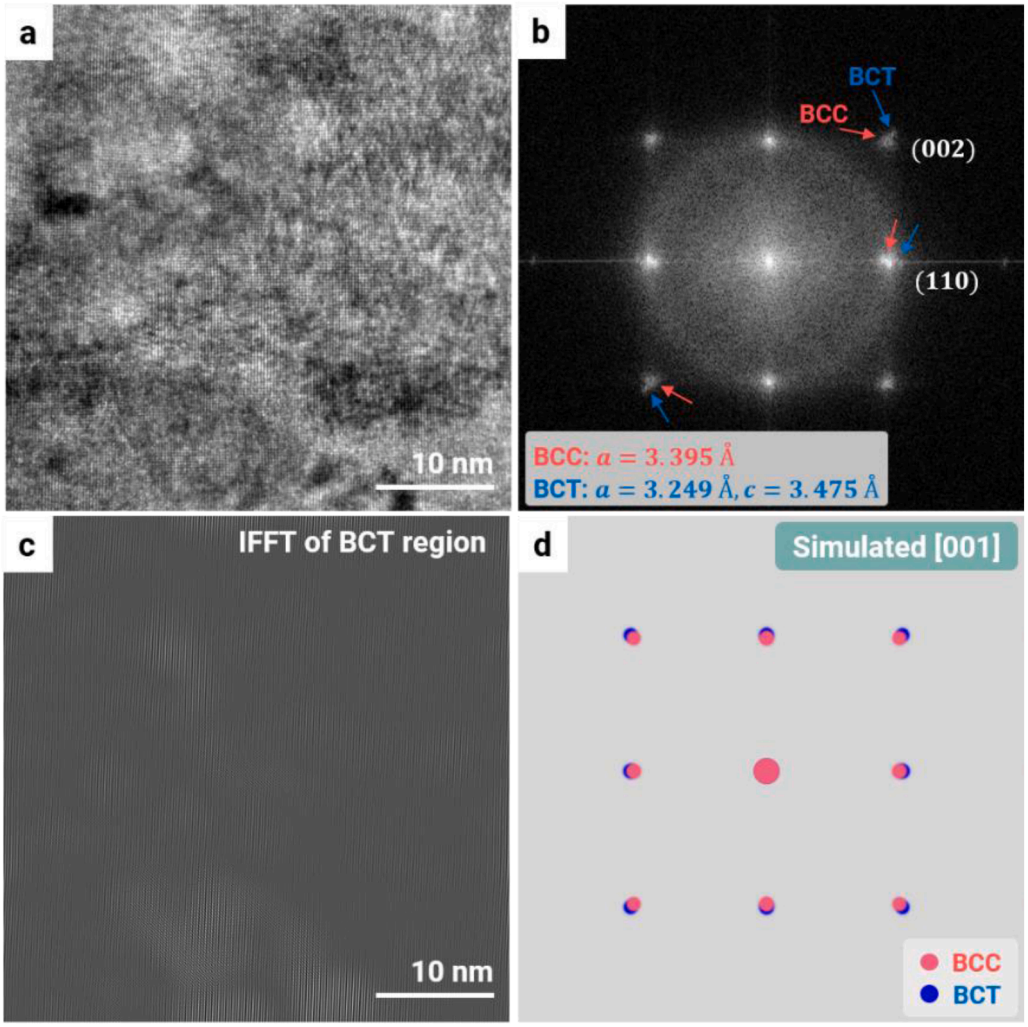

Fig. 6. (a) A representative high-resolution TEM (HRTEM) image of TiNbZr powder after the heat treatment in H_2 with a zone direction of [001], along with (b) its corresponding Fast Fourier transform (FFT) pattern and (c) inverse FFT (IFFT) image of the body-centered tetragonal (BCT) crystal structure. (d) Simulated selected area electron diffraction (SAED) patterns showing the coexistence of BCC and BCT crystal structures along the [001] zone axis.

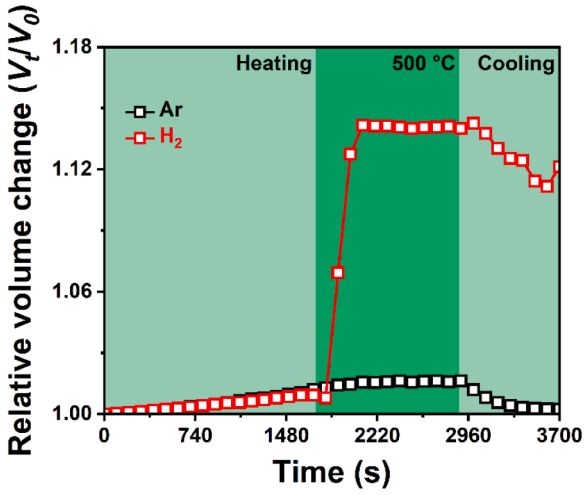

Fig. 7. Relative volume change of the crystal lattices in TiNbZr samples treated in H_2 and Ar.

displayed in Fig. 8. The treatment causes no obvious change in the shape and surficial morphology of particles due to the low heat treatment temperature (500 °C) and short treatment time (0.5 h). The particle size is measured to be 22.90±0.44 μm, consistent with that of the pristine state (Fig. 2c). The dendritic microstructure remains, as revealed in the cross-sectional SEM images (Fig. 8d). In addition, the chemical fluctuation of individual elements between interdendritic and dendritic regions is the same as that in the pristine sample (Fig. 8e). Such unchanged microstructure features are mainly attributed to the slow diffusion of the refractory elements at 500 °C (T/T_m = ~0.29, where T_m is the liquidus temperature of TiNbZr. As shown in **Fig. S15**, T_m is determined to be ~1720 °C by Thermo-Calc in conjunction with the thermodynamics database TCTI2). Despite the random orientation of grains after the treatment in H_2 (Fig. 8f), an increasing number of low-angle grain boundaries (2–15° misorientation) is observed, accounting for 46.2 % over all the boundaries (which is 16.2 %, and 19.6 % for the pristine sample and the sample after heat treatment under Ar (**Fig. S16**), respectively). Additionally, the local KAM value at these low-angle grain boundaries in the hydrogen-treated sample can reach values up to 2.04° as compared with 0.69° in the sample treated in Ar. The density of the geometric necessary dislocation (ρ) can be approximated following the equation, $\rho = \frac{3\times KAM}{b\times \Delta x}$, where b and Δx represent the magnitude of the Burgers vector and step size used for the EBSD scan, respectively [70, 71]. After the heat treatment in hydrogen, the dislocation density (7.07

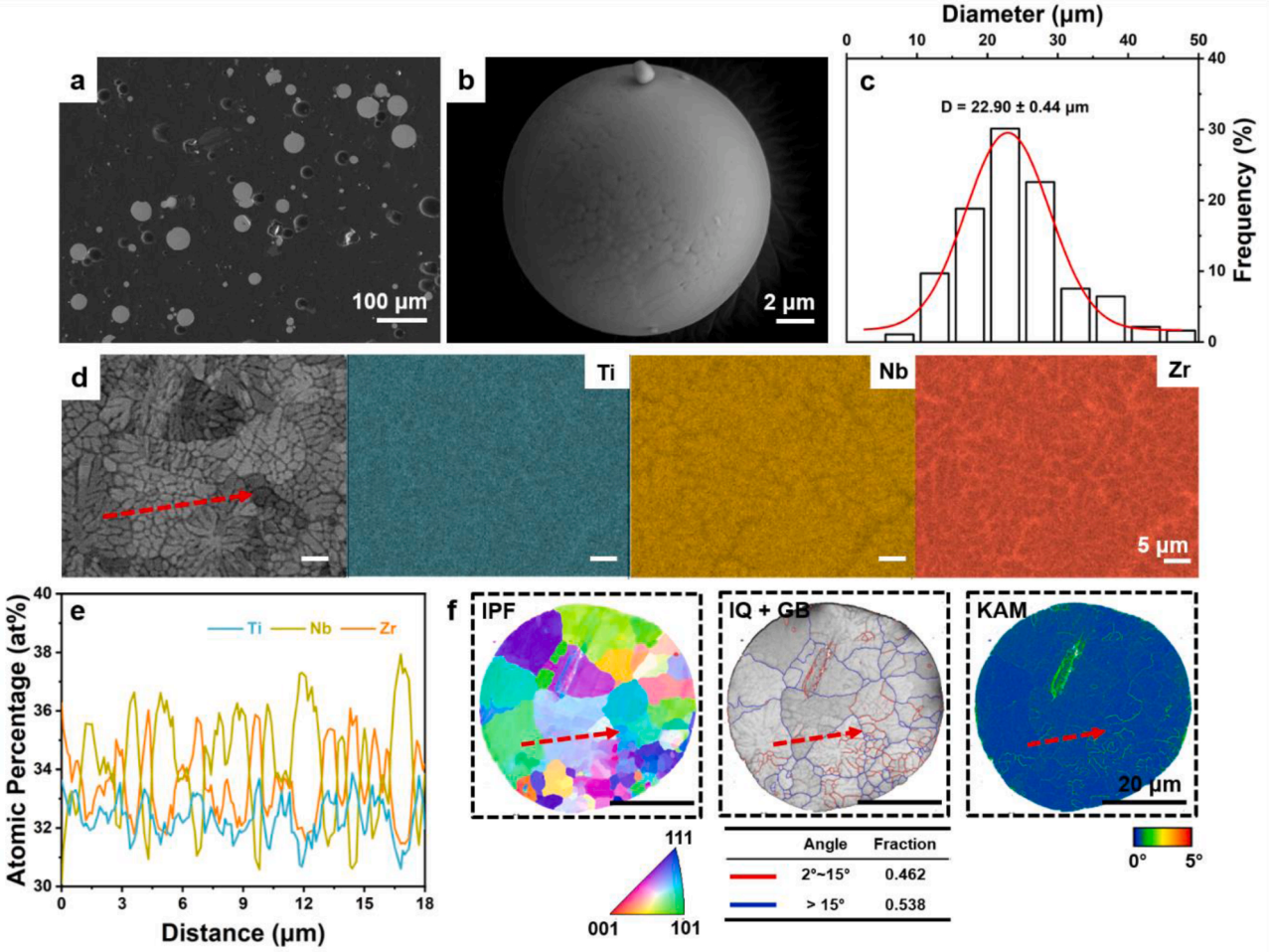

Fig. 8. Secondary electron images of (a) TiNbZr particles and (b) an individual TiNbZr particle after the treatment in H_2. (c) Size distribution of the TiNbZr particles. (d) Backscattered electron imaging of a particle and the corresponding elemental maps of Ti, Nb, and Zr probed by electron dispersive spectroscopy. (e) Elemental distribution across dendrites, as marked by the red arrow in (d). (f) Inverse pole figure (IPF), image quality overlaid with grain boundaries (IQ + GB), and kernel average misorientation (KAM) maps of the particle probed by the electron backscatter diffraction. The red arrow in (f) represents the same scan in (d).

$\times 10^{15}$ m^{-2}) is about three times higher than the reference sample (2.39 $\times 10^{15}$ m^{-2}), suggesting the significant internal distortion and associated strain localization caused by hydrogen ingress. The formation of low-angle grain boundaries can be attributed to the accommodation of the internal stress induced by hydrogen interstitials [19,72,73]. Specifically, the incorporation of a substantial amount of hydrogen solutes (>40 at.%) into the lattice induces a crystal structure transition from BCC to BCT. The presence of hydrogen solutes and the associated structural transformation result in significant lattice distortion, leading to the build-up of misfit dislocations. As these dislocations accumulate and multiply, they relax the local stresses by reorganizing into low-angle grain boundaries. Interestingly, these low-angle grain boundaries are distributed along the interdendritic regions, where Ti and Zr are enriched, which is mainly ascribed to the higher affinity of hydrogen to Ti and Zr than to Nb [56].

4. Discussion

The results presented in Section 3 show the evolution of the TiNbZr crystal lattice upon hydrogen uptake, *i.e.*, the isotropic lattice expansion during isothermal treatment in H_2 at 500 °C and followed by an anisotropic lattice expansion during the cooling schedule to room temperature. In this section, we discuss the preferred occupancy site of hydrogen atoms in the BCC lattice of TiNbZr alloy and the origin of the anisotropic tetragonal expansion of the lattice, to better understand the effect of hydrogen atoms on crystal structures. As listed in **Table S1**, TiNbZr undergoes a similar BCC-to-FCC phase transformation as most of the refractory M/HEAs at high pressure of hydrogen, underscoring the suitability of TiNbZr as a model material. Additionally, the simplicity of TiNbZr among the refractory M/HEA family facilitates the study, particularly in DFT-based simulations. The obtained result can provide valuable reference points for other refractory M/HEA systems.

4.1. Site occupancy of hydrogen atoms in the TiNbZr crystal lattice

The fundamental question is what the favorable accommodation site of one single hydrogen atom in the crystal lattice is, *i.e.*, devoid of any sublattice or Zener ordering correlations with other hydrogen atoms. The TiNbZr lattice with its BCC structure possesses two types of interstitial sites that can accommodate hydrogen atoms, namely, 12 tetrahedral sites and 6 octahedral sites per conventional BCC unit cell [54]. For the following qualitative and geometry-based discussion, the reasoning is built on the simple BCC rigid lattice, with geometric considerations applied to tetrahedral and octahedral sites. Generally, the radius (r) of a tetrahedral site (0.291 R, R is the radius of the host metal atom) is approximately twice that of an octahedral site (0.155 R) [54]. Because of the larger accommodation space of a tetrahedral site in the TiNbZr alloy (calculated to be 0.426 Å, considering a lattice parameter of 3.3836 Å from Fig. 1), intuitively, a hydrogen atom (with a radius of 0.53 Å) should prefer to occupy a tetrahedral site rather than an

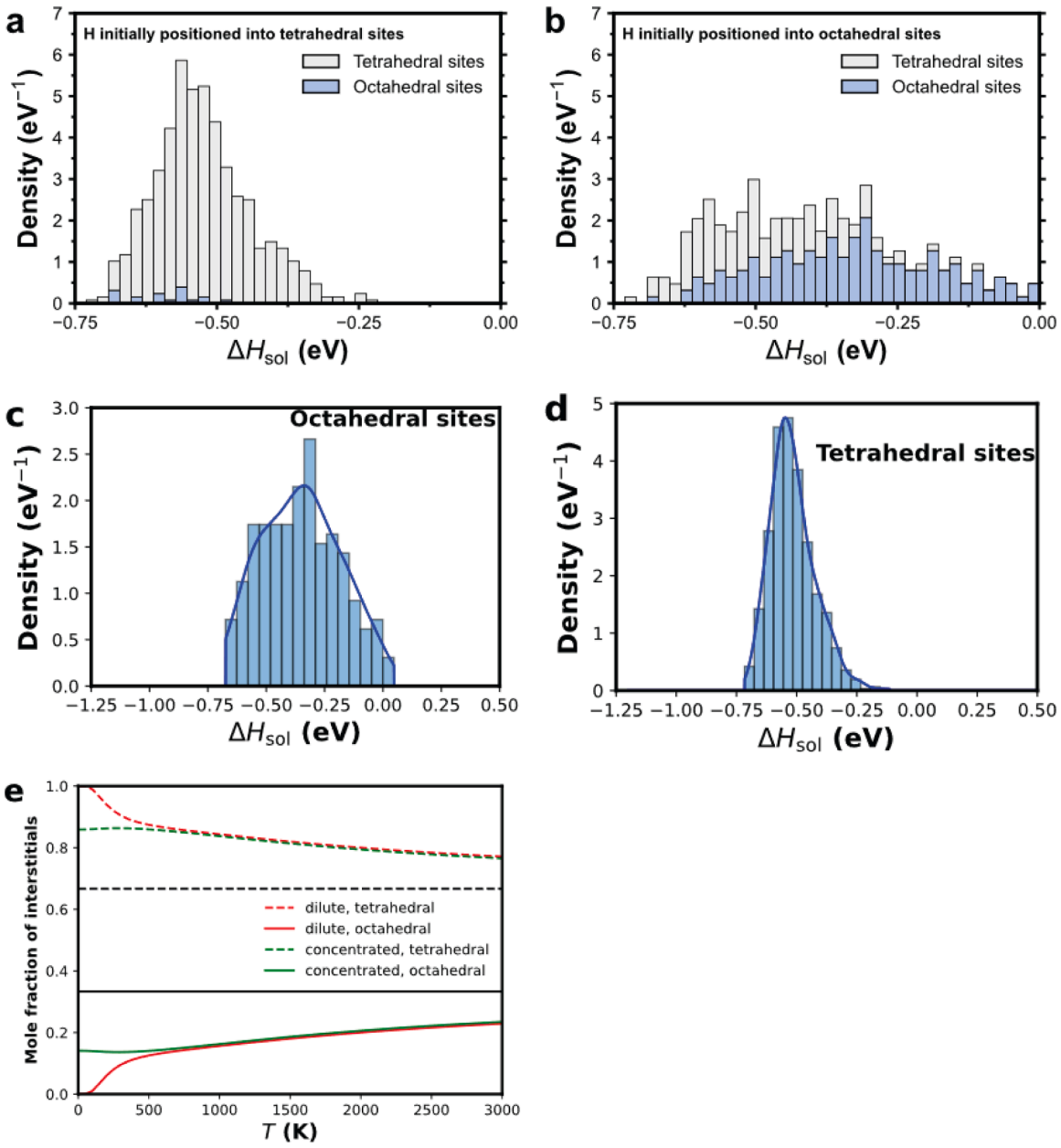

Fig. 9. Statistical distribution of the solution enthalpy per hydrogen atom in a TiNbZr special quasirandom supercell after a full stress relaxation with one hydrogen atom initially positioned at all possible (a) octahedral interstitial sites and (b) tetrahedral interstitial sites. Corresponding distribution of relaxed hydrogen states in (c) octahedral and (d) tetrahedral sites. DFT calculations were conducted with a 3 × 3 × 3 conventional supercell (54 metallic atoms) at T=0 K. (e) Calculated frequency for the tetrahedral and octahedral occupancy assuming a Fermi-Dirac distribution of energy states in the case of dilute and concentrated hydrogen solution corresponding to 1 and 45 hydrogen atoms in the supercell, respectively (hydrogen mole fraction: 2 at.% and 45.4 at.%, respectively).

octahedral site [29,68,74,75]. The validity of this hypothesis is further rationalized by DFT calculations (Fig. 9). We therefore computed the hydrogen solution energies on the various symmetry inequivalent interstitial tetrahedral and octahedral sites in the constructed TiNbZr SQS supercell. After the relaxation of the atomic positions, about half of the considered octahedral sites turned out to be unstable: the hydrogen occupies a neighboring tetrahedral site (Fig. 9a). In contrast, the considered tetrahedral sites were almost all stable, and we observed that only for a few cases relaxation into an octahedral position after the full stress relaxation (Fig. 9b). Having the energy distribution over the different sites and knowing that a single site can only be occupied by a single hydrogen atom, we can use the Fermi-Dirac statistics to calculate the ratio of hydrogen in tetrahedral *vs*. octahedral sites as a function of temperature (T) and hydrogen concentration (X_H) [76]. Since a single interstitial site can accommodate no more than one single hydrogen atom, the statistics describing the hydrogen distribution is given by Fermi-Dirac distribution,

$$f(\Delta H_{sol}; T, \mu) = \left[\exp\left(\frac{\Delta H_{sol} - \mu}{k_B T}\right) + 1\right]^{-1} \quad (2)$$

where ΔH_{sol} is the solution energy of a hydrogen interstitial on a specific site, and μ, k_B, and T stand for the chemical potential of hydrogen, Boltzmann constant, and temperature, respectively. The total hydrogen concentration x (relative to the total number of available interstitial sites (*i.e.*, tetrahedral and octahedral sites)) is given by,

$$\int_{-\infty}^{+\infty} n(\Delta H_{sol}) f(\Delta H_{sol}; T, \mu) d\Delta H_{sol} = x \quad (3)$$

where the density of states $n(\Delta H_{sol})$ has been determined from energies calculated by DFT for various interstitial sites for a single hydrogen atom. Eqs. (2) and (3) are solved self-consistently to obtain the hydrogen chemical potential $\mu(T, x)$ for a given hydrogen concentration. As revealed in Fig. 9e, for a dilute hydrogen concentration (corresponding to a single hydrogen atom in the SQS supercell with 54 metallic atoms), $T = 0$ K gives almost 100 % of tetrahedral occupancy. Higher temperature gives a lower tendency to occupy the tetrahedral sites, asymptotic to an approximately 2:1 ratio of the number of tetrahedral and octahedral interstitials when the temperature approaches infinitely large values. Over the temperature of interest, more than 80 % of tetrahedral occupancy is the result. Thus, the above DFT calculations strongly indicate that tetrahedral sites are energetically preferable to accommodate a hydrogen atom no matter whether it is initially introduced to a tetrahedral or octahedral site. Such a preference for hydrogen accommodation at tetrahedral sites is in line with the previous studies in the literature with low hydrogen concentrations [68,77,78]. It is worth noting that the impact of the zero-point energy on the hydrogen binding energy is negligible. Explicit calculations showed that it gives rise to only very subtle contributions (−0.01 to 0.03 eV/H-atom) to the solution energies (~0.4 eV/H-atom) (**Fig. S17**). Additionally, unstable octahedral sites at T=0 K may be dynamically stabilized by temperature, including thermal vibrations and electronic excitations. However, given that this would require significantly computationally expensive molecular dynamics simulations, we consider this to be beyond the scope of the present work.

Next, we discuss the scenario where a large number of hydrogen atoms are present. The Fermi-Dirac distribution of energy states gives a similar trend of the temperature-dependent tetrahedral occupancy when 45 hydrogen atoms are present in the supercell (corresponding to the saturated hydrogen concentration, following the experimental results shown in Fig. 7) except for the low-temperature region (<500 K) where the tetrahedral hydrogen stabilized at around 85 % of occupancy. Nevertheless, the tetrahedral sites remain the preferred positions for the hydrogen atoms (Fig. 9e). It is worth noting that the above Fermi-Dirac analysis is suited mainly for qualitative interpretation. Three main assumptions have been made for the Fermi-Dirac analysis: (1) The volume change due to hydrogen is ignored, which might be important for cases where high hydrogen concentrations apply. (2) The predicted results for low hydrogen concentrations should be interpreted with caution, as they are highly sensitive to the sampling of the low-energy region. (3) The hydrogen-hydrogen interaction is neglected. To address these limitations, we explicitly introduced 45 randomly distributed hydrogen atoms in the supercell. For the sake of simplicity, a random distribution of hydrogen interstitials was assumed in the supercell using two different configurations with initial occupancy of all hydrogen atoms in only octahedral sites and only tetrahedral sites, respectively. In total, 200 different configurations with 45 hydrogen atoms have been considered for DFT calculations (**Table S7**). Specifically, two BCC SQS cells were utilized for DFT calculations, and we sampled 50 octahedral and 50 tetrahedral configurations for each SQS cell. The minimum distance of neighboring hydrogen-hydrogen bonds was constrained to values larger than 2.0 Å (see computed force and interactions between nearest-neighbor hydrogen atoms in **Fig. S18**) to avoid the large hydrogen-hydrogen repulsive interaction [29,75,79]. Fig. 10a shows the calculated solution enthalpy for the two cases before and after the full stress relaxation. For the former case, the presence of hydrogen interstitials on octahedral sites is unfavorable, as evidenced by the higher averaged solution enthalpy of 0.035 eV/H-atom than that (−0.469 eV/H-atom) of the tetrahedral configuration. Even after the full stress relaxation, the solution enthalpy of hydrogen atoms initially positioned at the octahedral sites remains higher (−0.336 eV/H-atom) compared with the latter case when hydrogen atoms are placed on the tetrahedral sites prior to relaxation. The solution enthalpy of the latter case with initial tetrahedral hydrogen configuration decreases further to −0.605 eV/H-atom upon full relaxation. Additionally, the volume expansion of the supercell is determined to be approximately 11.1±0.3 % after the incorporation of 45 hydrogen atoms (randomly distributed, see **Fig. S19**), consistent with the value derived from the HEXRD experiment. These results confirm that even at such a high concentration of hydrogen (46.4 at.% hydrogen), tetrahedral sites are more favorable sites for hydrogen accommodation. As tetrahedral interstitial sites reveal isotropic geometry, hydrogen atoms exert a uniform force on the nearest neighboring host atoms, leading to an isotropic expansion of the lattice [68]. When hydrogen atoms are randomly distributed at tetrahedral sites, they result in almost isotropic expansion of TiNbZr lattices with a small c/a ratio of 1.007 (Fig. 10b). This c/a ratio is consistent with the constructed SQS supercell without hydrogen atoms (1.006, due to finite size of the supercell). Such a case reflects the situation at an elevated temperature during the isothermal heat treatment process, where hydrogen atoms can be expected to be randomly distributed within the TiNbZr crystal

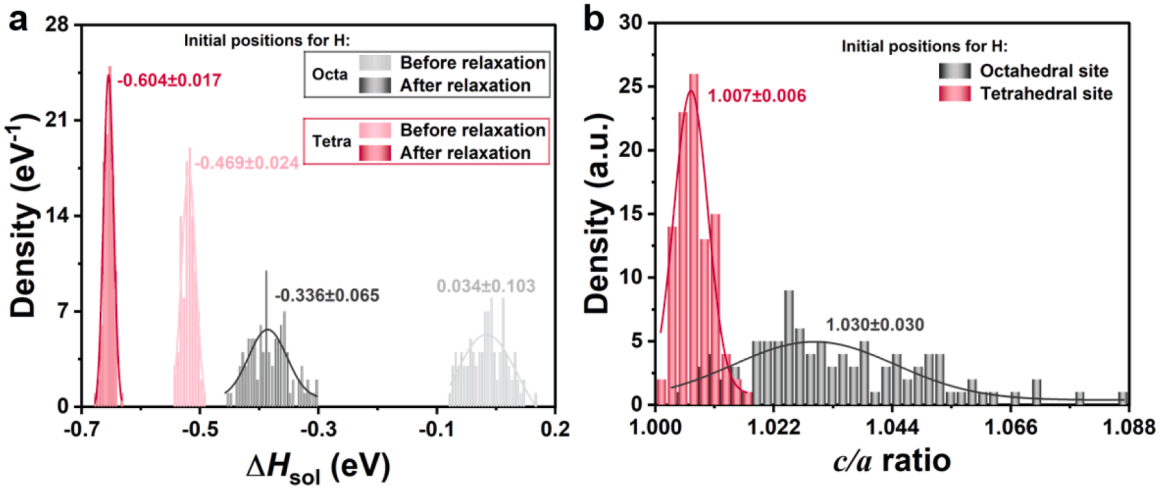

Fig. 10. (a) Statistical distribution of calculated solution enthalpy per hydrogen atom before and after atomic relaxation when 45 hydrogen atoms are positioned at octahedral or tetrahedral sites in a supercell with 54 metal atoms. The data has been obtained from DFT calculations. (b) Statistical distribution of calculated c/a ratio with all hydrogen initially settling at the tetrahedral and octahedral sites after relaxation based on DFT calculations. DFT calculations were conducted with a 3 × 3 × 3 conventional supercell (54 metallic atoms) at T=0 K.

due to the configurational entropy effect at high temperatures [29]. Thus, the current BCC structure is predominantly stable with hydrogen interstitials randomly distributed at the tetrahedral sites at a high temperature, as also suggested in the *in-situ* HEXRD experiments (Fig. 4).

4.2. Occurrence of lattice tetragonality upon cooling

An intriguing observation is the tetragonal distortion of the hydrogen-saturated crystal lattice upon cooling as determined by HEXRD and TEM methods (Figs. 5 and 6). The advantages and disadvantages of both methods shall be briefly summarized and discussed for the determination of tetragonality. HEXRD is commonly used in the detection of tetragonality, especially for the tetragonal distortion of Fe-C martensite [80,81]. For HEXRD, the X-ray diffractograms reflect the crystal structures averaged over the probed volume (here, ~0.4 mm^3) with excellent statistical information [80,81]. However, measuring tetragonality relies on indirect profile analysis of the peak splitting and broadening [82]. The uncertainty arising from the deconvolution of diffraction peaks (based on the least squares method) hinders its direct utility for interpreting tetragonality [82,83]. In contrast, the TEM-based electron diffraction technique provides local but direct information, despite the challenging and time-intensive preparation of thin films for TEM observations. Concerning the micro-size powder sample in this study, the focused ion beam (FIB) cutting method was used for the site-specific TEM lamella preparation, although it can unavoidably introduce artifacts during the thinning process, limiting the explanation of the results [84,85]. Therefore, in our study, a combination of HEXRD and TEM methods was employed to validate local lattice tetragonality, and to understand and minimize the inaccuracies resulting from relying solely on a single testing method. Both the occurrence of peak splitting and broadening in the HEXRD experiment, and the overlap of two diffraction spots in the TEM analysis strongly support the tetragonality of TiNbZr lattices upon cooling. Nevertheless, a slight variation of c/a ratios is observed for the sample measured using the two methods (ranging from 1.06 for HEXRD to 1.07 for TEM). Such a discrepancy in the c/a ratios might be due to the spatial/angular resolution limit associated with these two techniques, one being local (TEM) and the other integral (HEXRD).

The presence of tetragonality upon cooling indicates a change in the configuration of hydrogen atoms in the accommodation sites, which results in an asymmetric lattice expansion (expansion along the c-axis in this study). Based on the hydrogen concentration (~46.4 at.%) and the presence of tetragonality, two reasonable atomic configurations are considered (Fig. 11a). For the sake of simplicity, we only consider scenarios where hydrogen atoms occupy a single type of interstitial site, either a tetrahedral or octahedral site. Scenario I: all hydrogen interstitials are positioned at tetrahedral sites with a specific hydrogen occupancy of $(0, \frac{1}{2}, \frac{1}{4})$ and $(0, \frac{1}{2}, \frac{3}{4})$, as these sites are calculated to be the energetically favorable positions for hydrogen accommodation (see Section 4.1). Although a tetrahedral hydrogen atom applies uniform force on four neighboring metallic atoms, the specific arrangement of the hydrogen atoms in a lattice can result in a joint force along the c-axis, thus causing an asymmetric lattice expansion [68]. Scenario II: all

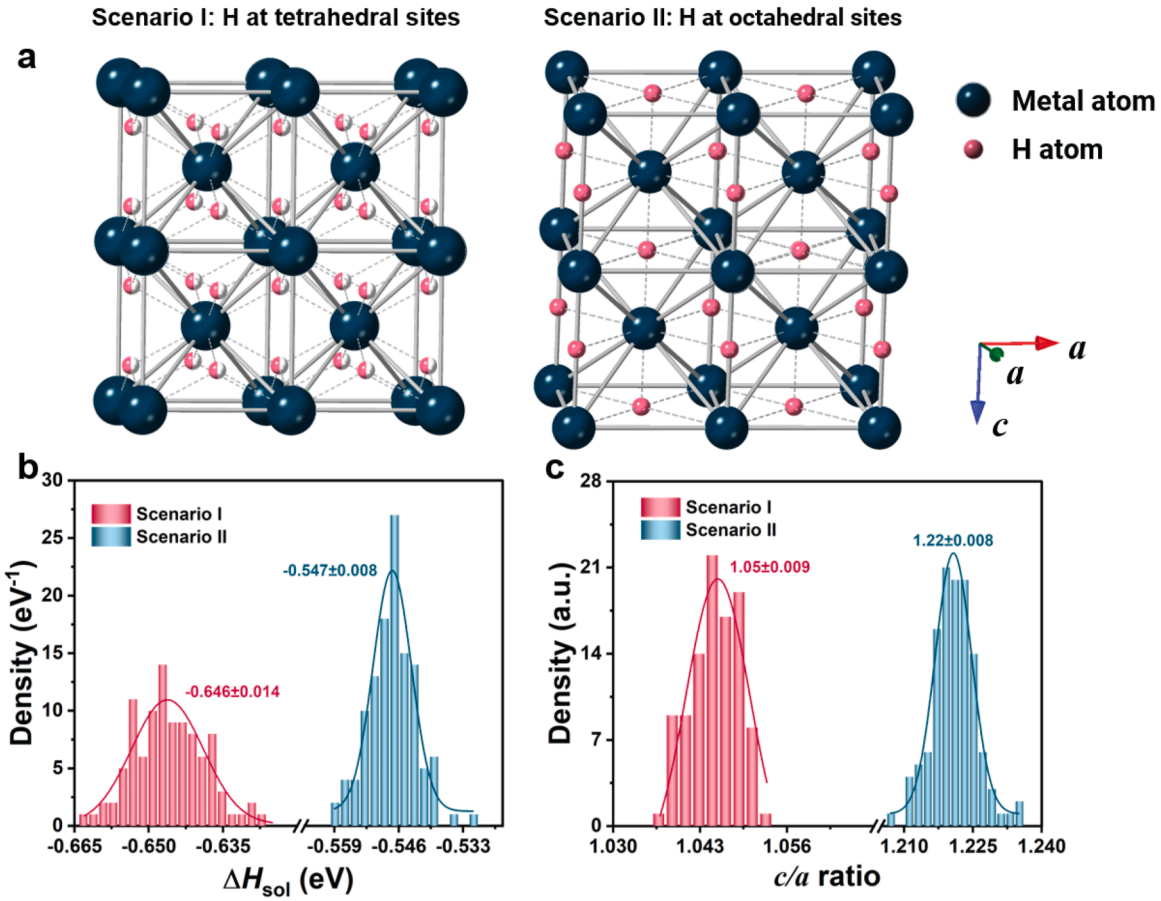

Fig. 11. (a) The proposed lattice configurations, which are possible to result in lattice tetragonality, namely, the asymmetric expansion along the c-axis. Scenario I with all hydrogen atoms positioned at the tetrahedral $(0, \frac{1}{2}, \frac{1}{4})$ and $(0, \frac{1}{2}, \frac{3}{4})$ sites (In this case, only half of the marked sites are occupied by hydrogen atoms), while all hydrogen atoms are located at the octahedral sites (hydrogen occupancy: $(0, 0, \frac{1}{2})$ and $(\frac{1}{2}, \frac{1}{2}, 0)$) in Scenario II. Statistical distribution of (b) calculated solution enthalpy per hydrogen atom and (c) calculated c/a ratio of Scenario I and Scenario II after stress relaxation. DFT calculations were conducted with a $3 \times 3 \times 3$ conventional supercell (54 metallic atoms) at T=0 K.

hydrogen interstitials are positioned at octahedral sites with an ordering distribution (hydrogen occupancy: (0, 0, $\frac{1}{2}$) and ($\frac{1}{2}$, $\frac{1}{2}$, 0)). In comparison to the tetrahedral hydrogen atoms, octahedral hydrogen interstitials exert a non-uniform force, exhibiting higher forces on the two nearest neighboring atoms [68]. Owing to these ordered distributions of hydrogen interstitials, a reduction of the total energy of the system is expected [29]. This hypothesis will be further testified through *ab initio* DFT calculations.

To validate the tetragonal distortion caused by the ordering distribution of hydrogen atoms, all of them were located in tetrahedral or octahedral sites within the lattices. It is noted that the solution enthalpy of the Scenario I configuration reaches a lower value (−0.646±0.014 eV/H-atom) compared with the Scenario II (−0.547±0.008 eV/H-atom) (Fig. 11b), suggesting a more stable configuration for hydrogen accommodation. The difference in configurational entropy between random solid solution (in tetrahedral sites) and Scenario I configuration (under the ideal mixing assumption, see supplementary materials Note 1) is determined to be $\Delta S_{conf} \approx 1.24 k_B$ per hydrogen atom. With this value, the phase transformation temperature of Scenario I from a random solid solution is predicted to be 382 K. Since other factors, such as composition variations, exchange-correlation functionals, and thermal vibrations, will also contribute to the transition temperature, this predicted temperature is in qualitative agreement with the BCT-2 transition temperature observed in the HEXRD experiment (~723 K). Simultaneously, the *c/a* ratio of Scenario I is determined to be 1.05 ±0.009 (Fig. 11b), in agreement with that of the predominant BCT-2 crystal structure (~1.06) as evidenced by the HEXRD result (Fig. 5). Although the Scenario II configuration exhibits a higher solution enthalpy, the *c/a* ratio with 1.22±0.008 is in line with the BCT-1 crystal structure (~1.22). This result implies that the Scenario II configuration, in which all hydrogen atoms are periodically positioned at the octahedral sits, is likely to be an intermediate configuration. This configuration is considered to be a transformable state from BCC to FCC during the hydrogenation [14,15]. Such octahedral occupancy of hydrogen atoms is thought to increase the disorder of hydrogen-hydrogen bonds, thus destabilizing the BCC crystal structure and inducing subsequent phase transformation. This metastable nature also explains why the Scenario II configuration with a *c/a* ratio of ~1.22 is challenging to be detected when using TEM characterization techniques, which were conducted several weeks after the *in-situ* HEXRD experiment. The underpinning physics leading to the presence of tetragonality upon cooling are mainly due to, (1) the occupation of a tetrahedral (or octahedral) site which produces an elongation of the *c*-axis, which, in turn, facilitates the occupancy of neighboring tetrahedral (or octahedral) sites by other hydrogen atoms, a phenomenon referred to as collective interstitial ordering [29]; (2) the local anharmonicity in the strain fields induced by interstitials, which substantially stabilizes the collective ordering [86].

In this study, a single-step BCC-to-BCT transformation is observed in the TiNbZr alloy upon cooling from 500 °C after hydrogenation (1 bar H_2). In the literature, a fully hydrogenated TiNbZr at 40 bar H_2 reveals a FCC crystal structure [87], which is a typical hydride phase in TiNbZr-based HEAs (**Table S1**). Notably, a different transformation pathway is also observed for some alloys with similar compositions, forming BCT hydride as the fully hydrogenated form, *e.g.* in TiVZrNbTa [88]. The discrepancy in transformation pathways can be attributed to: (1) Composition difference: Alloys appearing to form BCT metal hydrides often contain vanadium (V), where V tends to stabilize the BCT hydride phase at high hydrogen concentrations [29,89]. Moreover, in the case of group IV elements (*i.e.*, Ti, and Zr in this study), tetragonal lattice distortions can be observed at hydrogen concentrations exceeding 60 at.% hydrogen [90,91]. Refractory M/HEAs with a high proportion of these elements have a high tendency to form BCT hydrides; (2) Lattice distortion (δ): Variations in δ, calculated as $\delta = \sqrt{\sum_i c_i \left(1 - \frac{r_i}{\bar{r}}\right)^2} \times 100$, where c_i, and r_i denote the atomic fraction, and the radius of element i respectively, while $\bar{r}$ stands for the averaged atomic radius, can also influence the transformation pathway [14,92]. This parameter is closely related to the availability of the interstitial sites within lattices. Here, TiNbZr have a δ value of 4.3 %, aligning with a classical BCC-to-FCC transformation that is typical for alloys with small δ values. In contrast, TiVNbZrTa, which forms BCT hydrides, has a δ value of 5.8 %. Refractory M/HEAs with high δ values are accompanied with more available interstitial sites (especially for octahedral sites) within the lattice. The large lattice distortion can lead to the reduction in the energy barrier for hydrogen octahedral accommodation. The occupancy of octahedral sites can induce the elongation of the *c*-axis, thus favoring the formation of BCT hydrides. While these factors suggest a connection between phase transformations and composition/lattice distortion, establishing a quantitative relationship remains challenging. Additional physicochemical parameters, *i.e.*, valence electron concentration (VEC), electronegativity (δ_x), might also influence phase transformation pathways [14,87].

4.3. Preference of hydrogen accommodation towards Ti/Zr

It is also worth noting that an increase in the fraction of low-angle grain boundaries is found after the treatment in H_2 (Figs. 2 and 8). Even though heat treatment typically results in recovery of low-angle grain boundaries [93,94], the increase in their presence in this study is primarily attributed to the volume change and lattice distortion associated with the uptake of hydrogen atoms within TiNbZr lattices. More specifically, the hydrogen atoms, especially in a high concentration, can severely distort the lattice structure, leading to the subsequent generation of low-angle grain boundaries [19,56,72,73]. Moreover, these newly formed low-angle grain boundaries are mainly distributed along the Ti and Zr-rich interdendritic regions (Fig. 8), supporting the fact that hydrogen exhibits a higher tendency towards Ti and Zr rather than Nb due to the lower mixing enthalpy [56]. This tendency is also known from their mixtures (*e.g.*, hydride) according to the elementary phase diagram (*i.e.*, Ti-H), where only phase diagrams of Nb+H, Zr+H, and Ti+H systems have been experimentally assessed or evaluated using the CALPHAD (CALculation of PHAse Diagram) method [90,91,95]. The partial molar enthalpy of hydrogen solution in β-Ti is nearly −59.4 kJ/mol as compared with 43.0 kJ/mol for that of Nb, indicating the higher affinity of hydrogen to Ti than that to Nb. A similar trend can be obtained for Zr (partial molar enthalpy of hydrogen solution in β-Zr is −74.5 kJ/mol), suggesting a higher affinity to hydrogen for Zr as compared with Nb. Our DFT calculations also revealed that the solution enthalpy of hydrogen is lower when more nearest neighboring Ti atoms are present (Fig. 12). The solution enthalpy drops from 0.23 eV/H-atom to approximately −0.32 eV/H-atom as the number of nearest neighboring Ti atoms increases from 0 to 2 for octahedral hydrogen interstitials. A similar trend is found for the tetrahedral hydrogen interstitials, with the lowest solution enthalpy of −0.63 eV/H-atom when surrounded by 4 nearest neighboring Ti atoms. The Nb atoms, however, exhibit an opposite effect on hydrogen interstitials compared with Ti. The solution enthalpy associated with hydrogen increases with the number of nearest neighboring Nb atoms, while Zr exhibits similar behavior as Ti. These findings are important, suggesting that the local chemical environment provided by the surrounding host alloying atoms can entail local hydrogen preference (*i.e.*, where the hydrogen is preferably stored or less preferably stored). The same fact applies to the kinetic barriers when extracting the hydrogen atoms from the metal again for generating hydrogen molecules [7,96,97]. Translated to the application of such MEAs as high-temperature materials exposed to hydrogen (*e.g.*, combustion engines), this fact also means that specific lattice regions enriched in Ti, Zr, or both might be particularly susceptible to an embrittling effect due to such hydrogen-induced local

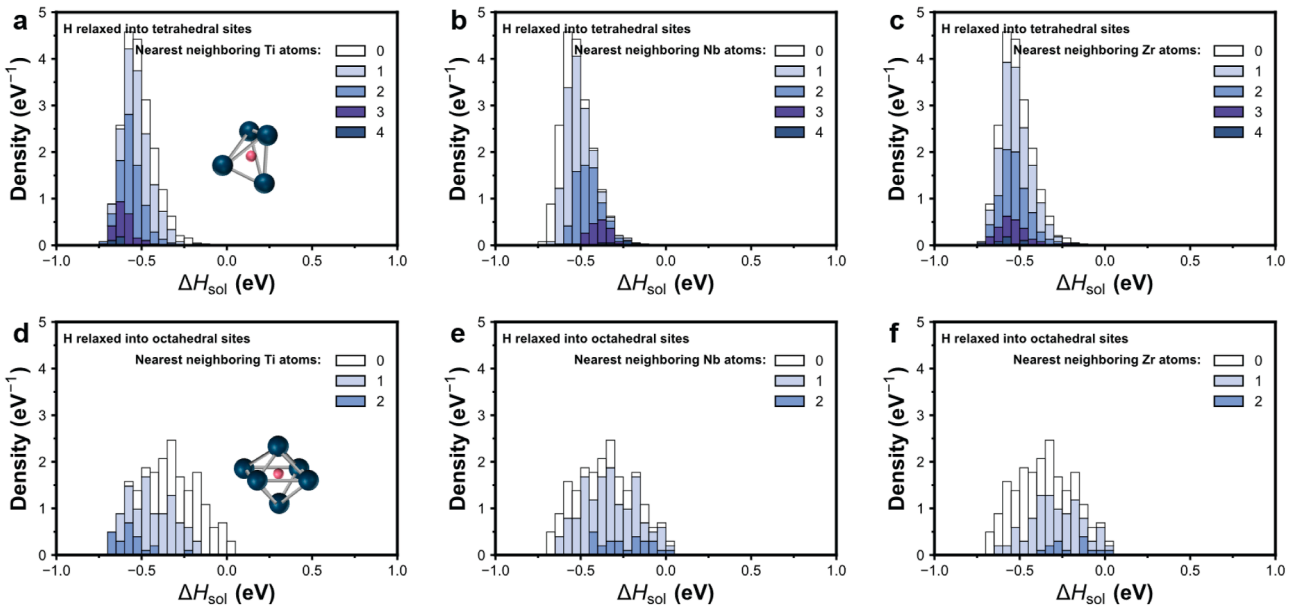

Fig. 12. Calculated statistical distribution of the hydrogen solution enthalpy per hydrogen atom of TiNbZr with one hydrogen solute relaxed to either tetrahedral interstitial sites or octahedral interstitial sites surrounded by different amounts of nearest neighbor (a, d) Ti atoms, (b, e) Nb atoms and (c, f) Zr atoms. DFT calculations were conducted with a 3 × 3 × 3 conventional supercell (54 metallic atoms) at T=0 K.

distortion.

5. Conclusions

This study investigated the real-time microstructural evolution of TiNbZr alloy during the heat treatment in pure hydrogen using *in-situ* synchrotron high-energy X-ray diffraction combined with density functional theory calculations to understand the hydrogen accommodation down to the atomic scale. The main conclusions are:

(1) The body-centered cubic (BCC) lattice exhibited a significant isotropic expansion during hydrogen uptake at 500 °C, with a lattice volume increase of 4.845 $Å^3$ (corresponding to a hydrogen concentration of 46.4 at.%). It is worth noting that such a high hydrogen concentration did not induce the formation of hydrides, due to the comparably high solubility of hydrogen within these metallic elements. The DFT calculations revealed that tetrahedral sites were the energetically more favorable positions for hydrogen accommodation for both dilute and high concentrations of hydrogen.

(2) The hydrogen-saturated BCC crystal structure at 500 °C transformed into a body-centered tetragonal (BCT) structure upon cooling to room temperature. The transformation followed the dilatation-dominant displacive transformation pathway with a spontaneous lattice symmetry breaking and discontinuous lattice constant change. The presence of tetragonality is due to the change in the distribution of hydrogen interstitials. The ordered distribution of hydrogen interstitials along tetrahedral sites (hydrogen positioned in tetrahedral $(0, \frac{1}{2}, \frac{1}{4})$ and $(0, \frac{1}{2}, \frac{3}{4})$ sites) led to the asymmetric lattice expansion along the *c*-axis. This ordered distribution of hydrogen atoms during the structural evolution is attributed to the minimization of the system solution enthalpy as shown by DFT calculations. The underlying mechanisms resulting in tetragonality are mainly due to the collective interstitial ordering.

(3) Hydrogen atoms demonstrated a higher tendency to occupy Ti/Zr-rich interstitials compared with those surrounded by Nb atoms as analyzed from the elementary phase diagrams known from these mixtures (*e.g.*, Ti/Zr/Nb-H). As a consequence, a significant increase in the fraction of low-angle grain boundaries (by approximately 30.0 %) was found along Ti/Zr-enriched interdendritic regions after the heat treatment in H_2. The DFT calculations also revealed a higher affinity of hydrogen to Ti/Zr atoms as compared to its affinity to Nb atoms.

Thus, this study provides fundamental new insights into hydrogen accommodation in the interstitial positions in the TiNbZr medium-entropy alloy, highlighting its impact on the lattice symmetry and distortion. These findings shed light on the potential applications of this alloy class in the emerging hydrogen economy.

CRediT authorship contribution statement

Chengguang Wu: Writing – review & editing, Writing – original draft, Methodology, Investigation, Formal analysis, Data curation. **Yilun Gong:** Writing – review & editing, Supervision, Methodology, Investigation, Formal analysis. **Chang Liu:** Writing – review & editing, Methodology. **Xuehan Li:** Methodology. **Gökhan Gizer:** Writing – review & editing, Methodology. **Claudio Pistidda:** Writing – review & editing, Methodology. **Fritz Körmann:** Writing – review & editing, Methodology, Funding acquisition, Formal analysis. **Yan Ma:** Writing – review & editing, Supervision, Project administration, Conceptualization. **Jörg Neugebauer:** Writing – review & editing, Supervision, Methodology. **Dierk Raabe:** Writing – review & editing, Supervision, Project administration, Funding acquisition.

Declaration of competing interest

The authors declare that they have no known competing financial interests or personal relationships that could have appeared to influence the work reported in this paper.

Acknowledgments

The kind help on sample preparations and subsequent SEM-related characterizations from Monika Nellessen, Katja Angenendt, and Christian Broβ at the Max Planck Institute for Sustainable Materials is gratefully acknowledged. C.G.W. would like to acknowledge the

financial support from the China Scholarship Council (Number: 202106780003). Y.L.G., F.K., Y.M., and D.R. would like to acknowledge the financial funding of Deutsche Forschungsgemeinschaft (DFG) within the Priority Programme 2006 (Compositionally Complex Alloys—High Entropy Alloys, SPP2006-HEA-CCA). C.G.W. is also grateful to Dr. Shaolou Wei and Leonardo Shoji Aota for the lively discussion and technical exchange. Dr. Yuji Ikeda is acknowledged for providing the initial version of the Fermi-Dirac distribution analysis code. Parts of this research were carried out at PETRA III beamline P02.1 and we would like to thank Dr. Henrik Jeppesen for assistance in the HEXRD measurements. Beamtime was allocated for proposal I-20211077.

Supplementary materials

Supplementary material associated with this article can be found, in the online version, at doi:10.1016/j.actamat.2025.120852.

References

[1] D. Raabe, The materials science behind sustainable metals and alloys, Chem. Rev. 123 (5) (2023) 2436–2608.
[2] M.D. Allendorf, V. Stavila, J.L. Snider, M. Witman, M.E. Bowden, K. Brooks, B. L. Tran, T. Autrey, Challenges to developing materials for the transport and storage of hydrogen, Nat. Chem. 14 (11) (2022) 1214–1223.
[3] C. Pistidda, Solid-state hydrogen storage for a decarbonized society, Hydrogen 2 (4) (2021) 428–443.
[4] S.Eswarappa Prameela, T.M. Pollock, D. Raabe, M.A. Meyers, A. Aitkaliyeva, K.-L. Chintersingh, Z.C. Cordero, L. Graham-Brady, Materials for extreme environments, Nat. Rev. Mater. 8 (2) (2023) 81–88.
[5] A. Zuttel, Hydrogen storage methods, Naturwissenschaften 91 (4) (2004) 157–172.
[6] Y. Ma, Y. Ma, Q. Wang, S. Schweidler, M. Botros, T. Fu, H. Hahn, T. Brezesinski, B. Breitung, High-entropy energy materials: challenges and new opportunities, Energy Environ. Sci. 14 (5) (2021) 2883–2905.
[7] F. Marques, M. Balcerzak, F. Winkelmann, G. Zepon, M. Felderhoff, Review and outlook on high-entropy alloys for hydrogen storage, Energy Environ. Sci. 14 (10) (2021) 5191–5227.
[8] S. Wei, S.J. Kim, J. Kang, Y. Zhang, Y. Zhang, T. Furuhara, E.S. Park, C.C. Tasan, Natural-mixing guided design of refractory high-entropy alloys with as-cast tensile ductility, Nat. Mater. 19 (11) (2020) 1175–1181.
[9] M. Yan, W. Xu, M.S. Dargusch, H.P. Tang, M. Brandt, M. Qian, Review of effect of oxygen on room temperature ductility of titanium and titanium alloys, Powder Metall. 57 (4) (2014) 251–257.
[10] O.N. Senkov, J.M. Scott, S.V. Senkova, D.B. Miracle, C.F. Woodward, Microstructure and room temperature properties of a high-entropy TaNbHfZrTi alloy, J. Alloys. Compd. 509 (20) (2011) 6043–6048.
[11] C. Yang, S. Yang, L. Chen, H. Dong, X. Duan, C. Yu, W. Zhang, L. Liu, Low modulus Ti-rich biocompatible TiNbZrTaHf concentrated alloys with exceptional plasticity, Mater. Res. Lett. 11 (7) (2023) 604–612.
[12] L. Han, S. Zhu, Z. Rao, C. Scheu, D. Ponge, A. Ludwig, H. Zhang, O. Gutfleisch, H. Hahn, Z. Li, D. Raabe, Multifunctional high-entropy materials, Nat. Rev. Mater. 9 (12) (2024) 846–865.
[13] E.P. George, D. Raabe, R.O. Ritchie, High-entropy alloys, Nat. Rev. Mater. 4 (8) (2019) 515–534.
[14] C. Zlotea, M.A. Sow, G. Ek, J.P. Couzinié, L. Perrière, I. Guillot, J. Bourgon, K. T. Møller, T.R. Jensen, E. Akiba, M. Sahlberg, Hydrogen sorption in TiZrNbHfTa high entropy alloy, J. Alloys. Compd. 775 (2019) 667–674.
[15] M. Sahlberg, D. Karlsson, C. Zlotea, U. Jansson, Superior hydrogen storage in high entropy alloys, Sci. Rep. 6 (2016) 36770.
[16] X. Ma, X. Ding, R. Chen, W. Cao, Q. Song, Study on hydrogen storage property of (ZrTiVFe) xAly high-entropy alloys by modifying Al content, Int. J. Hydrogen. Energy 47 (13) (2022) 8409–8418.
[17] J. Hu, J. Zhang, H. Xiao, L. Xie, H. Shen, P. Li, J. Zhang, H. Gong, X. Zu, A density functional theory study of the hydrogen absorption in high entropy alloy TiZrHfMoNb, Inorg. Chem. 59 (14) (2020) 9774–9782.
[18] B. Sun, W. Krieger, M. Rohwerder, D. Ponge, D. Raabe, Dependence of hydrogen embrittlement mechanisms on microstructure-driven hydrogen distribution in medium Mn steels, Acta Mater. 183 (2020) 313–328.
[19] S. Jothi, T. Croft, S. Brown, Influence of grain boundary misorientation on hydrogen embrittlement in bi-crystal nickel, Int. J. Hydrogen. Energy 39 (35) (2014) 20671–20688.
[20] L. Huang, D. Chen, D. Xie, S. Li, Y. Zhang, T. Zhu, D. Raabe, E. Ma, J. Li, Z. Shan, Quantitative tests revealing hydrogen-enhanced dislocation motion in α-iron, Nat. Mater. 22 (6) (2023) 710–716.
[21] B. Sun, W. Lu, B. Gault, R. Ding, S.K. Makineni, D. Wan, C.-H. Wu, H. Chen, D. Ponge, D. Raabe, Chemical heterogeneity enhances hydrogen resistance in high-strength steels, Nat. Mater. 20 (12) (2021) 1629–1634.
[22] H. Zhao, P. Chakraborty, D. Ponge, T. Hickel, B. Sun, C.-H. Wu, B. Gault, D. Raabe, Hydrogen trapping and embrittlement in high-strength Al alloys, Nature 602 (7897) (2022) 437–441.
[23] C.A. Wert, Trapping of hydrogen in metals, in: G. Alefeld, J. Völkl (Eds.), Hydrogen in Metals II: Application-Oriented Properties, Springer Berlin Heidelberg, Berlin, Heidelberg, 1978, pp. 305–330.
[24] M.B. Djukic, G.M. Bakic, V. Sijacki Zeravcic, A. Sedmak, B. Rajicic, The synergistic action and interplay of hydrogen embrittlement mechanisms in steels and iron: localized plasticity and decohesion, Eng. Fract. Mech. 216 (2019) 106528.
[25] H. Luo, Z. Li, W. Lu, D. Ponge, D. Raabe, Hydrogen embrittlement of an interstitial equimolar high-entropy alloy, Corros. Sci. 136 (2018) 403–408.
[26] H. Luo, W. Lu, X. Fang, D. Ponge, Z. Li, D. Raabe, Beating hydrogen with its own weapon: nano-twin gradients enhance embrittlement resistance of a high-entropy alloy, Mater. Today 21 (10) (2018) 1003–1009.
[27] H. Luo, Z. Li, D. Raabe, Hydrogen enhances strength and ductility of an equiatomic high-entropy alloy, Sci. Rep. 7 (1) (2017) 9892.
[28] H. Luo, S.S. Sohn, W. Lu, L. Li, X. Li, C.K. Soundararajan, W. Krieger, Z. Li, D. Raabe, A strong and ductile medium-entropy alloy resists hydrogen embrittlement and corrosion, Nat. Commun. 11 (1) (2020) 3081.
[29] Y. Fukai, The metal-hydrogen system: basic bulk properties, in: Springer Science & Business Media, 2006.
[30] N. Peterson, Diffusion in refractory metals, in: Advanced Metals Research Corp Somerville MA, 1960.
[31] X. Wang, W. Guo, Y. Fu, High-entropy alloys: emerging materials for advanced functional applications, J. Mater. Chem. A 9 (2) (2021) 663–701.
[32] C. Zhang, A. Song, Y. Yuan, Y. Wu, P. Zhang, Z. Lu, X. Song, Study on the hydrogen storage properties of a TiZrNbTa high entropy alloy, Int. J. Hydrogen. Energy 45 (8) (2020) 5367–5374.
[33] M.M. Nygård, G. Ek, D. Karlsson, M. Sahlberg, M.H. Sørby, B.C. Hauback, Hydrogen storage in high-entropy alloys with varying degree of local lattice strain, Int. J. Hydrogen. Energy 44 (55) (2019) 29140–29149.
[34] S. Wei, J. Kang, C.C. Tasan, An *in situ* synchrotron X-ray study of reverse austenitic transformation in a metastable FeMnCo alloy, J. Mater. Res. 38 (2) (2022) 281–296.
[35] Y. Ma, W. Song, W. Bleck, Investigation of the microstructure evolution in a Fe-17Mn-1.5Al-0.3C steel via in situ synchrotron X-ray diffraction during a tensile test, Materials 10 (10) (2017).
[36] M.W. Davids, T. Martin, M. Lototskyy, R. Denys, V. Yartys, Study of hydrogen storage properties of oxygen modified Ti- based AB2 type metal hydride alloy, Int. J. Hydrogen. Energy 46 (25) (2021) 13658–13663.
[37] S. Yamanaka, T. Tanaka, M. Miyake, Effect of oxygen on hydrogen solubility in zirconium, J. Nucl. Mater. 167 (1989) 231–237.
[38] D. Peterson, B. Schlader, Solubility and diffusion of hydrogen in vanadium-oxygen alloys, Metall. Trans. A 19 (1988) 67–72.
[39] G. Welsch, R. Boyer, E. Collings, Materials properties handbook: titanium alloys, in: , 1993.
[40] A.-C. Dippel, H.-P. Liermann, J.T. Delitz, P. Walter, H. Schulte-Schrepping, O. H. Seeck, H. Franz, Beamline P02. 1 at PETRA III for high-resolution and high-energy powder diffraction, J. Synchrotron. Radiat. 22 (3) (2015) 675–687.
[41] U. Bösenberg, C. Pistidda, M. Tolkiehn, N. Busch, I. Saldan, K. Suarez-Alcantara, A. Arendarska, T. Klassen, M. Dornheim, Characterization of metal hydrides by in-situ XRD, Int. J. Hydrogen Energy 39 (18) (2014) 9899–9903.
[42] C. Pistidda, A. Santoru, S. Garroni, N. Bergemann, A. Rzeszutek, C. Horstmann, D. Thomas, T. Klassen, M. Dornheim, First direct study of the ammonolysis reaction in the most common alkaline and alkaline earth metal hydrides by *in situ* SR-PXD, J. Phys. Chem. C 119 (2) (2015) 934–943.
[43] B.H. Toby, R.B. Von Dreele, GSAS-II: the genesis of a modern open-source all purpose crystallography software package, J. Appl. Crystallogr. 46 (2) (2013) 544–549.
[44] P.E. Blöchl, Projector augmented-wave method, Phys. Rev. B 50 (24) (1994) 17953–17979.
[45] G. Kresse, J. Furthmüller, Efficient iterative schemes for ab initio total-energy calculations using a plane-wave basis set, Phys. Rev. B 54 (16) (1996) 11169.
[46] G. Kresse, J. Furthmüller, Efficiency of ab-initio total energy calculations for metals and semiconductors using a plane-wave basis set, Comput. Mater. Sci. 6 (1) (1996) 15–50.
[47] G. Kresse, D. Joubert, From ultrasoft pseudopotentials to the projector augmented-wave method, Phys. Rev. B 59 (3) (1999) 1758.
[48] J.P. Perdew, K. Burke, M. Ernzerhof, Generalized gradient approximation made simple, Phys. Rev. Lett. 77 (18) (1996) 3865.
[49] A. Baldereschi, Mean-value point in the Brillouin zone, Phys. Rev. B 7 (12) (1973) 5212.
[50] H.J. Monkhorst, J.D. Pack, Special points for Brillouin-zone integrations, Phys. Rev. B 13 (12) (1976) 5188.
[51] A. Zunger, S.-H. Wei, L. Ferreira, J.E. Bernard, Special quasirandom structures, Phys. Rev. Lett. 65 (3) (1990) 353.
[52] C. Zhang, Y. Wu, L. You, X. Cao, Z. Lu, X. Song, Investigation on the activation mechanism of hydrogen absorption in TiZrNbTa high entropy alloy, J. Alloys. Compd. 781 (2019) 613–620.
[53] C. Zhang, Y. Wu, L. You, W. Qiu, Y. Zhang, Y. Yuan, Z. Lu, X. Song, Nanoscale phase separation of TiZrNbTa high entropy alloy induced by hydrogen absorption, Scr. Mater. 178 (2020) 503–507.
[54] D.R. Askeland, P.P. Phulé, W.J. Wright, D. Bhattacharya, The science and engineering of materials, (2003).
[55] J. Jin, M. Liu, P. Lin, T. Fu, Y. Hao, H. Jin, Ultrahigh temperature processing by concentrated solar energy with accurate temperature measurement, Appl. Therm. Eng. 150 (2019) 1337–1344.
[56] A. Takeuchi, A. Inoue, Classification of bulk metallic glasses by atomic size difference, heat of mixing and period of constituent elements and its application to

characterization of the main alloying element, Mater. Trans. 46 (12) (2005) 2817–2829.
[57] A.K. Swarnakar, O. Van der Biest, B. Baufeld, Thermal expansion and lattice parameters of shaped metal deposited Ti–6Al–4V, J. Alloys. Compd. 509 (6) (2011) 2723–2728.
[58] Q. Li, K. Lin, Z. Liu, L. Hu, Y. Cao, J. Chen, X. Xing, Chemical diversity for tailoring negative thermal expansion, Chem. Rev. 122 (9) (2022) 8438–8486.
[59] J.A. Kaduk, S.J.L. Billinge, R.E. Dinnebier, N. Henderson, I. Madsen, R. Černý, M. Leoni, L. Lutterotti, S. Thakral, D. Chateigner, Powder diffraction, Nat. Rev. Methods Primers 1 (1) (2021).
[60] G. Gottstein, Physical Foundations of Materials Science, Springer, 2004.
[61] R.W. Balluffi, S.M. Allen, W.C. Carter, Kinetics of Materials, John Wiley & Sons, 2005.
[62] R. Feenstra, R. Griessen, D. De Groot, Hydrogen induced lattice expansion and effective HH interaction in single phase PdHc, J. Phys. F Metal Phys. 16 (12) (1986) 1933.
[63] M. Khanuja, B. Mehta, P. Agar, P. Kulriya, D. Avasthi, Hydrogen induced lattice expansion and crystallinity degradation in palladium nanoparticles: effect of hydrogen concentration, pressure, and temperature, J. Appl. Phys. 106 (9) (2009) 093515.
[64] G.K. Pálsson, A. Bliersbach, M. Wolff, A. Zamani, B. Hjörvarsson, Using light transmission to watch hydrogen diffuse, Nat. Commun. 3 (1) (2012) 892.
[65] E. Galindo-Nava, B. Basha, P. Rivera-Díaz-del-Castillo, Hydrogen transport in metals: integration of permeation, thermal desorption and degassing, J. Mater. Sci. Technol. 33 (12) (2017) 1433–1447.
[66] M. Yashima, K. Morimoto, N. Ishizawa, M. Yoshimura, Diffusionless tetragonal–cubic transformation temperature in zirconia–ceria solid solutions, J. Am. Ceram. Soc. 76 (11) (1993) 2865–2868.
[67] L. Delaey, Diffusionless transformations, Phase Transf. Mater. (2001) 583–654.
[68] Y. Fukai, Site preference of interstitial hydrogen in metals, J. Less Common Metals 101 (1984) 1–16.
[69] H. Pfeiffer, H. Peisl, Lattice expansion of niobium and tantalum due to dissolved hydrogen and deuterium, Phys. Lett. A 60 (4) (1977) 363–364.
[70] P.J. Konijnenberg, S. Zaefferer, D. Raabe, Assessment of geometrically necessary dislocation levels derived by 3D EBSD, Acta Mater. 99 (2015) 402–414.
[71] E. Breitbarth, S. Zaefferer, F. Archie, M. Besel, D. Raabe, G. Requena, Evolution of dislocation patterns inside the plastic zone introduced by fatigue in an aged aluminium alloy AA2024-T3, Mater. Sci. Eng. A 718 (2018) 345–349.
[72] Z.-H. Sung, M. Wang, A. Polyanskii, C. Santosh, S. Balachandran, C. Compton, D. Larbalestier, T. Bieler, P. Lee, Development of low angle grain boundaries in lightly deformed superconducting niobium and their influence on hydride distribution and flux perturbation, J. Appl. Phys. 121 (19) (2017) 193903.
[73] D.-G. Xie, L. Wan, Z.-W. Shan, Hydrogen enhanced cracking via dynamic formation of grain boundary inside aluminium crystal, Corros. Sci. 183 (2021) 109307.
[74] T. Ishimoto, M. Koyama, Theoretical study of tetrahedral site occupation by hydrogen in Pd nanoparticles, J. Chem. Phys. 148 (3) (2018) 034705.
[75] J. Li, B. Li, X. Yu, H. Zhao, H. Shao, Geometrical effect in Mg-based metastable nano alloys with BCC structure for hydrogen storage, Int. J. Hydrogen. Energy 44 (55) (2019) 29291–29296.
[76] Y. Ikeda, I. Tanaka, J. Neugebauer, F. Körmann, Impact of interstitial C on phase stability and stacking-fault energy of the CrMnFeCoNi high-entropy alloy, Phys. Rev. Mater. 3 (11) (2019) 113603.
[77] C. Moore, J. Wilson, M. Rushton, W. Lee, J. Astbury, S. Middleburgh, Hydrogen accommodation in the TiZrNbHfTa high entropy alloy, Acta Mater. 229 (2022) 117832.
[78] Y.A. Du, L. Ismer, J. Rogal, T. Hickel, J. Neugebauer, R. Drautz, First-principles study on the interaction of H interstitials with grain boundaries in α-and γ-Fe, Phys. Rev. B Condens. Matter Mater. Phys. 84 (14) (2011) 144121.
[79] D. Westlake, Hydrides of intermetallic compounds: a review of stabilities, stoichiometries and preferred hydrogen sites, J. Less Common Metals 91 (1) (1983) 1–20.
[80] Y. Lu, H. Yu, R.D. Sisson, The effect of carbon content on the c/a ratio of as-quenched martensite in Fe-C alloys, Mater. Sci. Eng. A 700 (2017) 592–597.
[81] M. Cadeville, J. Friedt, C. Lerner, Structural, electronic and magnetic properties of splat-quenched FeCx alloys (x≤ 0.05), J. Phys. F Metal Phys. 7 (1) (1977) 123.
[82] T. Tanaka, N. Maruyama, N. Nakamura, A.J. Wilkinson, Tetragonality of Fe-C martensite – a pattern matching electron backscatter diffraction analysis compared to X-ray diffraction, Acta Mater. 195 (2020) 728–738.
[83] G. Nolze, A. Winkelmann, G. Cios, T. Tokarski, Tetragonality mapping of martensite in a high-carbon steel by EBSD, Mater. Charact. 175 (2021).
[84] S. Zaefferer, A critical review of orientation microscopy in SEM and TEM, Cryst. Res. Technol. 46 (6) (2011) 607–628.
[85] J. Mayer, L.A. Giannuzzi, T. Kamino, J. Michael, TEM sample preparation and FIB-induced damage, MRS Bull. 32 (5) (2007) 400–407.
[86] X. Zhang, H. Wang, T. Hickel, J. Rogal, Y. Li, J. Neugebauer, Mechanism of collective interstitial ordering in Fe–C alloys, Nat. Mater. 19 (8) (2020) 849–854.
[87] G. Ek, M.M. Nygård, A.F. Pavan, J. Montero, P.F. Henry, M.H. Sørby, M. Witman, V. Stavila, C. Zlotea, B.C. Hauback, Elucidating the effects of the composition on hydrogen sorption in TiVZrNbHf-based high-entropy alloys, Inorg. Chem. 60 (2) (2020) 1124–1132.
[88] D. Karlsson, G. Ek, J. Cedervall, C. Zlotea, K.T. Møller, T.C. Hansen, J. Bednarcik, M. Paskevicius, M.H. Sørby, T.R. Jensen, Structure and hydrogenation properties of a HfNbTiVZr high-entropy alloy, Inorg. Chem. 57 (4) (2018) 2103–2110.
[89] L. Beavis, Characteristics of some binary transition metal hydrides, J. Less Common Metals 19 (4) (1969) 315–328.
[90] A. San-Martin, F. Manchester, The H− Ti (hydrogen-titanium) system, Bull. Alloy Phase Diagrams 8 (1) (1987) 30–42.
[91] E. Zuzek, J. Abriata, A. San-Martin, F. Manchester, The H-Zr (hydrogen-zirconium) system, Bull. Alloy Phase Diagrams 11 (4) (1990) 385–395.
[92] Y. Ye, Q. Wang, J. Lu, C. Liu, Y. Yang, High-entropy alloy: challenges and prospects, Mater. Today 19 (6) (2016) 349–362.
[93] S. Weissmann, M. Hirabayashi, H. Fujita, On the mechanical and thermal stability of low-angle boundaries in zinc single crystals, J. Appl. Phys. 32 (6) (1961) 1156–1164.
[94] H. Guo, Y. Zhao, Y. Sun, J. Tian, H. Hou, K. Qi, X. Tian, Phase field crystal study of grain boundary structure and annihilation mechanism in low-angle grain boundary, Superlattices. Microstruct. 129 (2019) 163–175.
[95] J.F. Smith, The H−Nb (Hydrogen-Niobium) and D−Nb (Deuterium-Niobium) systems, Bull. Alloy Phase Diagrams 4 (1) (1983) 39–46.
[96] S. Yang, F. Yang, C. Wu, Y. Chen, Y. Mao, L. Luo, Hydrogen storage and cyclic properties of (VFe) 60 (TiCrCo) 40-xZrx (0≤ x≤ 2) alloys, J. Alloys. Compd. 663 (2016) 460–465.
[97] M.M. Nygård, G. Ek, D. Karlsson, M.H. Sørby, M. Sahlberg, B.C. Hauback, Counting electrons-a new approach to tailor the hydrogen sorption properties of high-entropy alloys, Acta Mater. 175 (2019) 121–129.
[98] C. Wu, L.S. Aota, J. Rao, X. Zhang, L. Perrière, M.J. Duarte, D. Raabe, Y. Ma, Hydrogen-assisted spinodal decomposition in a TiNbZrHfTa complex concentrated alloy, Acta Mater 285 (2025) 120707.